PHYSICS OF FLUIDS **21**, 125106 (2009)

Characteristics of coherent vortical structures in turbulent flows over progressive surface waves

Di Yang and Lian Shen
Department of Civil Engineering, Johns Hopkins University, Baltimore, Maryland 21218, USA

(Received 20 January 2009; accepted 27 October 2009; published online 29 December 2009)

Vortical structures in turbulence over progressive surface waves are studied using the data from direct numerical simulation of a stress-driven turbulent Couette flow above a waving surface. Instantaneous flow field and its evolution, vorticity statistics, and conditionally averaged flow field with various sampling methods are examined. Unique vortical structures are identified, which are found to be strongly dependent on the wave motion. For a slow wave (with a small value of wave age $c/u_*=2$; here c is the phase speed of the wave and u_* is the friction velocity), the vortical structures are characterized by reversed horseshoe vortices and quasistreamwise vortices. The former is concentrated above the wave trough and is associated with sweep events there; the latter has high intensity over the windward face of the wave and is associated with ejection events. Relative to the waveform, the coherent vortical structures propagate in the downstream direction. Vortex turning and vortex stretching play an important role in the vortex transformation and evolution processes. For an intermediate wave ($c/u_*=14$) and a fast wave ($c/u_*=25$), the dominant vortical structure is bent quasistreamwise vortices, which are predominantly horizontal but have a distinctive downward bending in their upstream ends near the wave trough. The vortices are found to propagate in the upstream direction with respect to the waveform. The above-wave coherent vortices identified in this study are found to play an important role in the turbulent transport process. © *2009 American Institute of Physics*. [doi:10.1063/1.3275851]

I. INTRODUCTION

Turbulent flow over progressive surface wave is related to many important fluid problems. Examples include wind-wave generation and evolution, gas and heat transfer between the atmosphere and the oceans, and many industrial processes involving gas-liquid interfacial phenomena. To model and predict the flow properties in these applications, there is a critical need for the study of turbulence structures in the boundary layer over the wave, of which our current understanding is quite limited due to the complexities associated with the curved geometry of the wave surface and the orbital motion of the wave.

The displacement of a wavy surface provides a periodically curved boundary to the turbulent flow above it and generates alternating favorable and adverse pressure gradients in the flow. To investigate the effect of wavy surface geometry on the turbulence field, many researchers studied the problem of turbulence over a stationary wavy wall theoretically,[1] numerically,[2–7] and experimentally.[8,9] These studies showed that the alternating concave and convex of the wavy surface make the flow structures strongly dependent on the streamwise location relative to the waveform, and that the flow statistics along the wavy surface is substantially different from that of a flat wall boundary layer.

In addition to the geometrical effect of the wavy surface, the surface motion of the wave introduces direct disturbance to the velocity field of the turbulence. In the past several decades, considerable amount of research has been conducted on turbulent flows over progressive water surface waves, including theoretical analyses,[10–12] numerical simulations,[13–16] and field and laboratory measurements.[17–20] It has been found that as the wave phase speed increases, the turbulence structure differs significantly from that above a stationary wavy wall. The distributions of many turbulence quantities are found to be determined by the relative motion of the surface wave and the turbulence, which is often measured by the wave age c/u_*, defined as the ratio between the wave phase speed c and the friction velocity u_*. Therefore, turbulence over the stationary wavy wall can only be regarded as an approximation of the slow (young) wave case.

Recently, we performed direct numerical simulation (DNS) for a comprehensive study of turbulent flows over various wavy surfaces including stationary wavy wall, vertically waving wall, and Airy and Stokes waves with and without surface drift.[21] Wind over progressive water surface wave is the focus of our study. In Ref. 21, we investigated slow wave with $c/u_*=2$, intermediate wave with $c/u_*=14$, and fast wave with $c/u_*=25$. It is shown that the statistics of turbulence intensity, pressure, Reynolds stress, and budget of turbulent kinetic energy have large variations with the wave phase; and the variations are greatly affected by the wave age. In investigating these turbulence statistics, we observed the existence of coherent vortical structures above the wave. These vortical structures possess many unique features in their instantaneous appearance, e.g., the dominance of quasistreamwise vortices that are apparently characterized by the periodicity of the wave, and the presence of horseshoe vortices that have reversed head and leg positions compared to the ones typically seen in a flat wall boundary layer.[22–25]

These vortices were rarely reported in literature and are the subject of this paper.

We note that almost all of the previous studies on vortical structures near wavy boundaries considered stationary walls only. For flows over stationary boundaries with a single concave or convex, the formation and attenuation of quasistreamwise vortices were studied theoretically (see, e.g., Ref. 26), experimentally (see, e.g., Ref. 27), and numerically (see, e.g., Ref. 28). For the stationary wavy wall case, there exist a few numerical studies containing results of vortical structures. De Angelis *et al.*[4] showed that quasistreamwise vortices are associated with the streaky structures near the stationary wavy wall. They suggested that the quasistreamwise vortices are generated around the reattachment point on the upstream ridge of the wave crest due to the impact of the fluids toward the wall. Calhoun and Street[6] calculated the Görtler number associated with the Görtler instability mechanism[29] and proposed that the Görtler instability is responsible for the presence of the quasistreamwise vortices. By investigating successive snapshots of instantaneous flow fields, Tseng and Ferziger[7] followed the evolution of vortices and illustrated the processes of vortex breakdown and reconnection.

As mentioned earlier, the turbulence structure above the progressive surface waves differs significantly from that above the stationary wavy wall. For the progressive wave case, as an early attempt, Tokuda[30] performed a stability analysis for air flows over water waves and predicted that quasistreamwise vortices would be generated above the wave trough for strong winds (i.e., slow wave case) and above the wave crest for gentle winds (i.e., fast wave case). However, no direct observation or statistical evidence is available yet to support Tokuda's prediction.

In this paper, we investigate the coherent vortical structures above the slow, intermediate, and fast progressive surface waves using the DNS data of Yang and Shen.[21] The objectives of the present study are to identify the different characteristic vortices in flows of different wave ages, to quantify the geometrical features of these vortices, to illustrate their spatial occurrence with respect to the waveform, to show their correlation with turbulent momentum and scalar transport, and to elucidate their evolution processes of generation, transformation, and attenuation. For this purpose, we examine instantaneous flow field and its evolution, vorticity statistics, and conditionally averaged flow field with various sampling methods.

We organize this paper as follows. The problem definition and numerical method are discussed in Sec. II. The statistics, structures, and evolution of coherent vortical structures in the slow wave case are studied in detail in Sec. III. Parallel to Sec. III, Sec. IV presents the intermediate and fast wave cases, which share considerable similarities between the two but are distinctly different from the slow wave case. Section V discusses the relationship of the coherent vortical structures to the turbulent transport. Finally, conclusions are provided in Sec. VI.

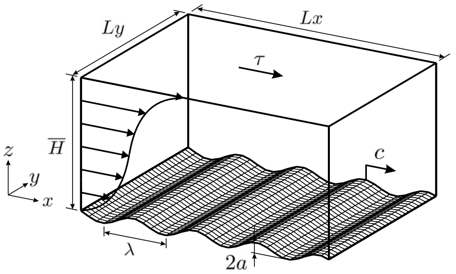

FIG. 1. Sketch of a three-dimensional turbulent Couette flow over a plane progressive surface wave. The turbulent flow is driven by a constant shear stress τ applied at the top boundary. The surface wave has a wavelength λ and an amplitude a. The wave propagates in the $+x$-direction with a phase speed c.

II. PROBLEM DEFINITION AND FLOW FIELD OVERVIEW

A. Problem definition

We consider a fully developed three-dimensional turbulent Couette flow over a plane progressive surface wave, as shown in Fig. 1. The flow is driven by a constant shear stress τ applied at the flat top boundary. The shear stress is related to the friction velocity by $\tau = \rho u_*^2$, where ρ is the fluid density. Periodic boundary conditions are used in the streamwise and spanwise directions. In our simulation, the Cartesian frame is fixed in space, with x, y, and z being the streamwise, spanwise, and vertical coordinates, respectively.

The turbulent flow motions are described by the incompressible Navier–Stokes equations

$$\frac{\partial u_i}{\partial t} + \frac{\partial u_i u_j}{\partial x_j} = -\frac{\partial p}{\partial x_i} + \frac{1}{\mathrm{Re}}\frac{\partial^2 u_i}{\partial x_j \, \partial x_j}, \tag{1}$$

$$\frac{\partial u_i}{\partial x_i} = 0. \tag{2}$$

Here, $u_i(i=1,2,3)=(u,v,w)$ are Cartesian velocity components in the x-, y-, and z-directions, respectively, and p is the dynamic pressure. Normalization is performed based on the wavelength of the surface wave λ and the mean velocity of the Couette flow at the top boundary U. The pressure p is normalized by ρU^2. The Reynolds number is defined as $\mathrm{Re} \equiv U\lambda/\nu$, with ν as the kinematic viscosity.

Surface water wave motion is used as the Dirichlet boundary condition at the wave surface for the simulation of the turbulent Couette flow over the wave. In our study, the wave motion is either prescribed based on wave theory or simulated together with the turbulence as a coupled system. For the vortical structures studied in this paper, these two approaches are found to yield similar results. The results we present in this paper are mainly for the prescribed wave case, but in Sec. III A we also present the results from the coupled simulation as comparison.

Here, we focus on the prescribed water wave boundary condition. The displacement and the velocity of the wave surface are given as

$$z_w = a \sin k(x - ct), \tag{3}$$

$$(u_w, v_w, w_w) = [akc \sin k(x-ct), 0, -akc \cos k(x-ct)]. \tag{4}$$

Here, z_w is the surface displacement of the wave, a is the amplitude of the surface wave, $k=2\pi/\lambda$ is the wavenumber, and u_w, v_w, and w_w are the streamwise, spanwise, and vertical components of the wave orbital velocity at the wave surface, respectively. In this study, the wave steepness is $ak=0.25$. In Eqs. (3) and (4), linear (sinusoidal) surface wave solution is used. As shown by Yang and Shen,[21] the wave nonlinearity as well as the surface drift affect some of the turbulence statistics. Here, we focus on the linear wave case mainly for the purpose of comparing with other studies on flows over wavy surfaces. In particular, almost all of the stationary wavy surface research in literature (reviewed in Sec. I) used sinusoidal waveform. Our comparison between linear and nonlinear wave cases, using the data of Yang and Shen[21] (results not shown here due to space limitation), and comparison between prescribed wave motion and turbulence-wave coupled simulation (cf. Sec. III A) confirm the results shown in this paper.

In Fig. 1, the surface wave propagates in the $+x$-direction, the same as the mean flow direction of the turbulent Couette flow. The effect of wave phase speed is quantified in terms of the wave age c/u_*. In the present study, we choose three different wave ages, $c/u_*=2$, 14, and 25. They are in the ranges of slow wave, intermediate wave, and fast wave in the problem of wind-wave interaction, respectively.[21,31]

B. Numerical method

In our simulation, we use a boundary-fitted grid system that enables the direct simulation of the turbulent flow down to the wave surface with the boundary layer resolved. The irregular surface-fitted physical space (x,y,z,t) is transformed to a rectangular computational space (ξ,ψ,ζ,τ) with the following algebraic mapping:

$$\tau = t, \quad \xi = x, \quad \psi = y, \quad \zeta = \frac{z-z_w}{H} = \frac{z-z_w}{\bar{H}-z_w}. \tag{5}$$

Here, the height of the physical domain H is decomposed into the average height $\bar{H}$ and a wave induced variation $-z_w$. The origin of the z-axis in the physical space is set at the mean surface level and the top boundary is at $z=\bar{H}$.

With Eq. (5), Eqs. (1) and (2) are rewritten in terms of the computational coordinates (ξ,ψ,ζ,τ). For spatial discretization, we use a Fourier series based pseudospectral method in the horizontal directions and a second-order finite-difference scheme on a clustered staggered grid[32] in the vertical direction. The governing equations are integrated in time by a fractional-step method.[33] We use a second-order Adams–Bashforth scheme for the convection terms and a Crank–Nicolson scheme for the viscous terms. The pressure Poisson equation is solved iteratively by a modified Newton's method.[32] Details of our numerical methods are provided in Refs. 32 and 21.

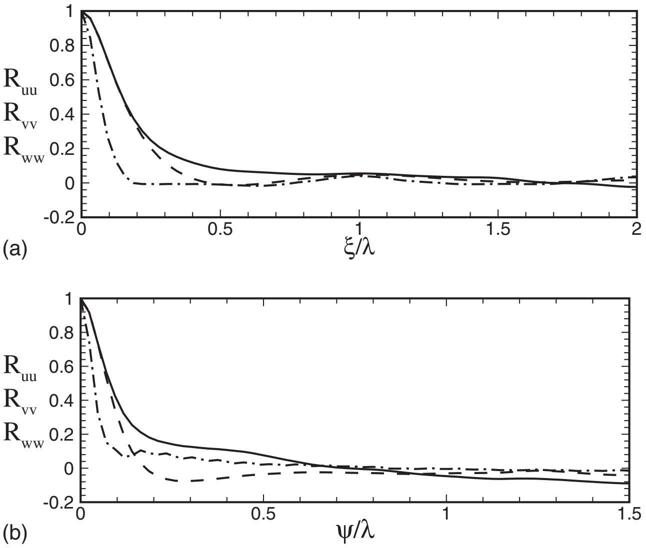

FIG. 2. Two-point correlation coefficient at $z^+=5$ above the wave surface $(c/u_*=2)$: —, R_{uu}; – –, R_{vv}; and –·–, R_{ww}. (a) Streamwise direction. (b) Spanwise direction.

In our DNS, the value of the Reynolds number is $\mathrm{Re}=U\lambda/\nu\approx 9189$. This corresponds to the Reynolds number based on the friction velocity, $\mathrm{Re}_*\equiv u_*\lambda/\nu\approx 283$. In terms of wall units, the wavelength of the surface wave is $\lambda^+\approx 283$. Here and hereafter, the superscript "+" denotes the velocity and length values normalized by wall variables u_* and ν/u_*, respectively.

The size of the computational domain is $4\lambda(\text{streamwise})\times 3\lambda(\text{spanwise})\times 2\lambda(\text{vertical})$. When using periodic boundary conditions in the horizontal directions, flow structures that exit from one end of the domain re-enter from the other end. To assure the domain size is sufficiently large, we have examined the two-point spatial correlation coefficients in both the streamwise and spanwise directions. The case of $c/u_*=2$ is plotted in Fig. 2 as an example. The values fall off to negligibly small within half of the domain lengths (2λ streamwise and 1.5λ spanwise), in a way similar to those in the literature.[28,34] In addition, we found that in the streamwise direction, the correlation coefficients at one-quarter of the domain size $(\xi/\lambda=1)$ decay faster than those in the flat surface case due to the disruption by the surface wave motion that has a wavelength of λ. Therefore, we conclude that the domain size chosen in our simulation is sufficiently large to apply the periodic boundary condition, and the inlet condition is not a concern in our simulation.

In both the streamwise and spanwise directions, we use an evenly spaced grid with 128 points in each direction; in the vertical direction, we use 129 grid points that are clustered toward the bottom and top boundaries. With this grid resolution, we have uniform grid spacing in the two horizontal directions $\Delta\xi^+=8.84$ and $\Delta\psi^+=6.63$, and vertical grid spacing $\Delta\zeta^+=0.42$ near the top and bottom boundaries, and $\Delta\zeta^+=8.45$ in the middle of the channel. In our simulation, the dissipative scale $\eta=(\nu^3/\varepsilon)^{1/4}$ based on the averaged dissipation rate ε (e.g., Ref. 34) is about two wall units. This grid resolution, though still larger than the estimated Kolmogorov scale, is shown to be sufficient to capture the es-

TABLE I. Resolution used in DNS of turbulent channel flow.

	Resolution in wall unit			Resolution in Kolmogorov scale		
Channel type	Δx^+	Δy^+	Δz^+	$\Delta x/\eta$	$\Delta y/\eta$	$\Delta z/\eta$
Curved channel[a]	18	6	0.2–8.2	11.25	3.75	0.13–5.1
Plane channel[b]	12	7	0.05–4.4	7.5	4.4	0.03–2.8
Stationary wavy wall[c]	16.8	8.4	0.1–4.2			
	8.4	8.4	0.1–4.2			
Water wave[d]	10.8	13.5	1.0–5.5			
Water wave[e]	8.84	6.63	0.42–8.45	4.5	3.4	0.2–4.3

[a] Reference 28.
[b] Reference 34.
[c] Reference 4.
[d] Reference 13.
[e] Present.

sential turbulent motions (see, e.g., Ref. 28). Our grid resolution is comparable to other DNS studies of turbulence over flat and wavy surfaces in literature. Table I shows the comparison.

Figure 3 shows an example of energy spectra, where k_x and k_y are the wavenumbers (normalized by $2\pi/L_x$, where L_x is the streamwise domain size) in the streamwise and spanwise directions, respectively. The energy spectra show that the energy density at high wavenumbers is several orders lower than that at low wavenumbers and there is no energy pileup at high wavenumbers, which indicates that the grid resolution is adequate. Note that the peak of E_{ww} at $k_x=4$ in Fig. 3(a) is associated with the surface wave, which has a wavenumber of $k=4$. Similar energy density peak has also been observed by previous studies (e.g., Ref. 4).

For the statistical results shown in this paper, to show the wave effect, we follow Hussain and Reynolds[35] and decompose a random variable f in the wave-following reference frame as $f(x,y,z,t)=\langle f\rangle(x,z)+f'(x,y,z,t)$. Here $\langle f\rangle$ is the phase-averaged value of f obtained by calculating ensemble average at fixed phase with respect to the surface wave and f' is the turbulence fluctuation. With the phase average, only one period in the streamwise direction is necessary when the statistics of turbulence is represented. However, for a better visualization of the turbulence structures, we plot two periods instead in some figures.

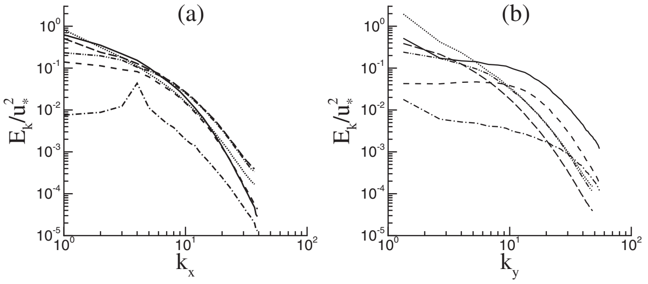

FIG. 3. One-dimensional energy spectra above the wave surface for the intermediate wave case ($c/u_*=14$). At $z^+=4.7$: —, E_{uu}; – – –, E_{vv}; and –·–, E_{ww}. At $z^+=146.3$: ····, E_{uu}; – –, E_{vv}; and –··–, E_{ww}. (a) Streamwise direction. (b) Spanwise direction.

In the present study, the computation has been carried out for about 13 500 viscous time units (tu_*^2/ν) after the turbulence has fully developed. Statistics are obtained from 160 instantaneous flow field data within $tu_*^2/\nu \in (9000, 13\,500)$ with time interval of about 27 viscous time units. This time interval is two times of the large-eddy turnover time τ_{turnover} (which is defined as the averaged turbulent kinetic energy divided by the dissipation rate),[36] hence the repeating sampling of individual structures is avoided. Meanwhile, this time interval differs from the period of the surface wave (35, 5, and 2.8 for the slow, intermediate, and fast waves, respectively) to make sure that the sampling is not at repeating wave period.

C. Vortices overview

This paper focuses on the coherent vortical structures in the turbulent Couette flow over the surface wave. In the past few decades of study on turbulence, a number of vortex identification schemes have been developed, among which the λ_2 method has been widely used in previous studies and has been cross validated with other methods.[37–39] In the λ_2 method, λ_2 is the second largest eigenvalue of the tensor $\mathbf{S}^2+\mathbf{\Omega}^2$, where $\mathbf{S}$ and $\mathbf{\Omega}$ are the symmetric and antisymmetric parts of the velocity gradient tensor $\nabla\mathbf{u}$, respectively. Following Jeong and Hussain,[37] we define the region with λ_2 smaller than a negative threshold as the interior of a vortex core.

To better illustrate the effect of surface wave on vortex dynamics, in the remainder of this paper we present our results in a frame traveling at the wave phase speed in the $+x$-direction. As shown in Fig. 4, since the wave phase speed is larger than the wave orbital velocity [i.e., $c>akc$ in Eq. (4)], fluid particles in the vicinity of the wave surface travel in the $-x$-direction in the wave-following frame. Compared to the slow wave case, the vertical extent of this reversed flow region is relatively larger for the immediate and fast wave cases. As a result, relative to the waveform, the near-surface vortical structures convected by the Couette flow travel in the $+x$-direction for $c/u_*=2$, but in the $-x$-direction for $c/u_*=14$ and 25. As will be shown in the subsequent sections, the difference in the relative motion of the vortices

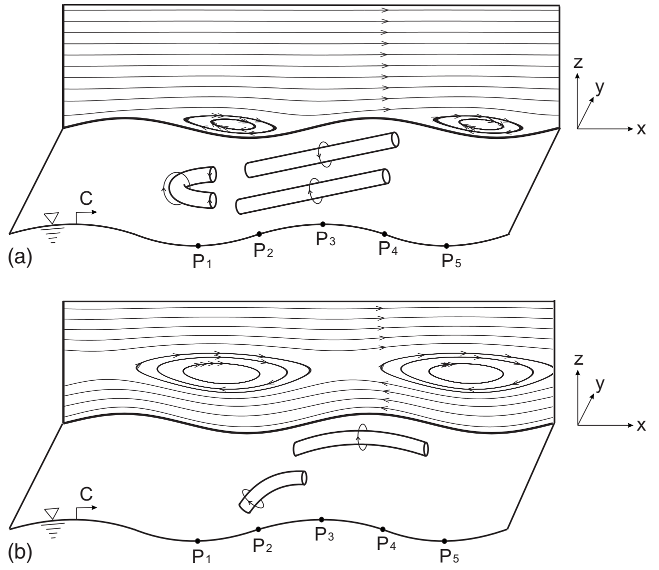

FIG. 4. Sketch of vortical structures above (a) slow wave $(c/u_*=2)$ and (b) intermediate wave $(c/u_*=14)$. The mean streamlines in the wave-following frame are plotted on the (x,z)-planes for both cases. The arrow next to c denotes the wave propagation direction in the fixed frame. In the wave-following frame, the surface waveform is stationary.

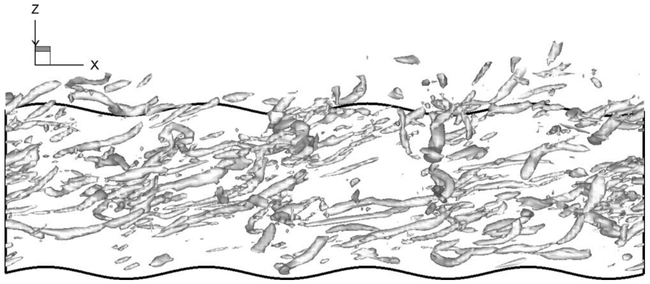

FIG. 5. Snapshot of near-surface coherent vortical structures in the turbulence field over the slow wave $(c/u_*=2)$. The vortical structures are identified by the isosurface of $\lambda_2=-1.0$.

with respect to the waveform results in disparate vortex dynamics between the slow and intermediate/fast wave cases. In Fig. 4(b), only the intermediate wave case is shown. The streamline pattern of the fast wave case is similar to that in the intermediate case, except that the location of the cat's eyes[12] is higher. The vortical structures above the fast wave is also similar to those above the intermediate wave, and the comparison between these two cases will be given in Sec. IV A.

Hereinafter, we define the streamwise direction based on the wave propagation direction for all the cases, i.e., the $+x$-direction is referred to as the *downstream* direction and the $-x$-direction is referred to as the *upstream* direction. As shown in Fig. 4, the surface wave is marked by five reference positions: P_1 and P_5 denote the wave troughs, P_3 denotes the wave crest, and P_2 and P_4 denote the upstream and downstream nodes of the wave, respectively, where the wave surface intersects the mean surface level. Based on these five reference positions, different sections of the wave surface are referred to as follows: (1) $\overset{\frown}{P_1P_3}$: windward face; (2) $\overset{\frown}{P_3P_5}$: leeward face; (3) $\overset{\frown}{P_1P_2}$: the slope downstream of the wave trough; (4) $\overset{\frown}{P_4P_5}$: the slope upstream of the wave trough; (5) $\overset{\frown}{P_2P_3}$: the slope upstream of the wave crest; and (6) $\overset{\frown}{P_3P_4}$: the slope downstream of the wave crest. In the following sections of this paper, the above terms are used to describe the positions of the vortical structures and other turbulence quantities with respect to the waveform.

III. COHERENT VORTICAL STRUCTURES ABOVE THE SLOW WAVE

In this section, we study the characteristics of coherent vortical structures above the slow wave $(c/u_*=2)$. Figure 5 shows the instantaneous vortical structures near the wave surface. It is found that the dominant vortical structures are the quasistreamwise vortices, which have the primary dimension along the streamwise direction. Most of these quasistreamwise vortices are located above the windward face $[\overset{\frown}{P_1P_3}$ in Fig. 4(a)], i.e., left of the wave crest in Fig. 5. Some of them extend over the crest to above the leeward face $[\overset{\frown}{P_3P_5}$ in Fig. 4(a)]. The streamwise size of these vortices is apparently constrained by the underlying wave, with the longest vortices comparable to the wavelength. In addition to these quasistreamwise vortices, there exist reversed horseshoe vortices near the wave trough. Opposite to the horseshoe vortices often observed in turbulence boundary layers, these reversed ones have their heads upstream but legs downstream. For the current case, it is found that about 26% of horseshoe vortices have the "forward" shape, while about 74% of them have the "reversed" shape. Yang and Shen[21] conjectured that the characteristic vortical structures in flows over slow waves are coherent quasistreamwise and reversed horseshoe vortices, as sketched in Fig. 4(a). In this section, we examine the features of the vortical structures by means of vorticity statistics, conditional average, and evolution observation.

A. Statistics of vortical structures above the slow wave

The occurrence of the quasistreamwise and reversed horseshoe vortices can be shown through the statistics of vortex inclination angles (see, e.g., Ref. 23). In this study, the two-dimensional inclination angles of the streamwise direction to the projections of the vorticity vector in (x,z)- and (x,y)-planes are defined as $\theta_{xz}=\tan^{-1}(\omega_z/\omega_x)$ and $\theta_{xy}=\tan^{-1}(\omega_y'/\omega_x)$, respectively, with the sign convention for the angles shown in Fig. 6. The statistics of the inclination

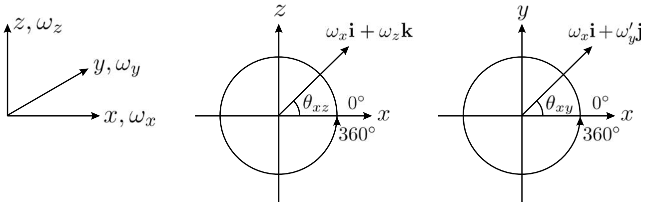

FIG. 6. Sign convention for vorticity inclination angles θ_{xz} and θ_{xy}. Here, θ_{xz} is the angle from the $+x$-axis to $\omega_x\mathbf{i}+\omega_z\mathbf{k}$ in the (x,z)-plane; θ_{xy} is the angle from the $+x$-axis to $\omega_x\mathbf{i}+\omega_y'\mathbf{j}$ in the (x,y)-plane.

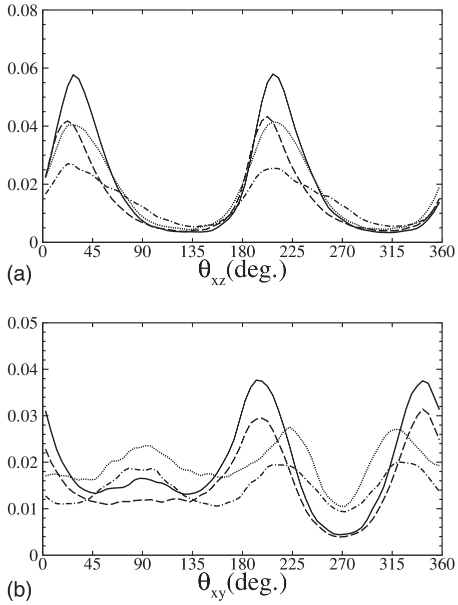

FIG. 7. Probabilities of two-dimensional vorticity angles at four streamwise locations above the slow wave ($c/u_* = 2$): —, windward face; – – –, crest; –·–, leeward face; and ····, trough. The vertical heights are chosen to be the locations of peak F_x, as shown in Fig. 8. Here, θ_{xz} is the angle from the $+x$-axis to the vorticity $\omega_x\mathbf{i}+\omega_z\mathbf{k}$; θ_{xy} is the angle from the $+x$-axis to the vorticity $\omega_x\mathbf{i}+\omega_y'\mathbf{j}$.

angles are weighted by the magnitudes of the respective projected vorticity vectors.[23] For vortices in the (x,y)-plane, the vorticity fluctuation ω_y' is used to exclude the mean shear in the boundary layer.

Figure 7 shows the probabilities of θ_{xz} and θ_{xy}. We consider four streamwise locations, which are above the windward face, crest, leeward face, and trough, respectively. Above the windward face, θ_{xz} is concentrated around 30° and 210°, and θ_{xy} is concentrated around 195° and 345°. The distribution of θ_{xz} indicates that the vortices are mainly horizontal, with an inclination to the upward direction following the wave surface upstream of the wave crest. The concentration of θ_{xy} indicates the dominance of streamwise vorticity, which corresponds to the quasistreamwise vortices above the windward face of the wave; it also indicates that the vorticity vectors with the opposite signs of ω_x tilt to the opposite sides of the x-axis in the (x,y)-plane. Above the crest, the concentration of θ_{xz} shifts slightly toward the x-axis to be around 25° and 205°, while the concentration of θ_{xy} shifts slightly away from the x-axis to be around 200° and 340°.

Above the leeward face and above the trough, θ_{xz} is concentrated around 25° and 205°, and θ_{xy} is concentrated mainly around 220° and 320°. In addition, there also exists a concentration of θ_{xy} around 90°, which corresponds to the spanwise vortical structures (i.e., the heads of reversed horseshoe vortices), as shown in Fig. 5.

To quantify the spatial frequency of the occurrence of the quasistreamwise and reversed horseshoe vortices, we define four detection functions as

$$I_0(x,y,z,t) = \begin{cases} 1 & \text{if } \lambda_2(x,y,z,t) \le 0, \\ 0 & \text{otherwise}, \end{cases} \tag{6}$$

$$I_x(x,y,z,t) = \begin{cases} 1 & \text{if } \sqrt{\omega_x^2+\omega_z^2} > |\omega_y| \quad \text{and} \quad |\omega_x| > |\omega_z|, \\ 0 & \text{otherwise}, \end{cases} \tag{7}$$

$$I_y(x,y,z,t) = \begin{cases} 1 & \text{if } \sqrt{\omega_x^2+\omega_z^2} < |\omega_y|, \\ 0 & \text{otherwise}, \end{cases} \tag{8}$$

$$I_z(x,y,z,t) = \begin{cases} 1 & \text{if } \sqrt{\omega_x^2+\omega_z^2} > |\omega_y| \quad \text{and} \quad |\omega_x| < |\omega_z|, \\ 0 & \text{otherwise}. \end{cases} \tag{9}$$

Here, I_0 detects the vortex core, and I_x, I_y, and I_z detect vortices pointing primarily in the x-, y-, and z-directions, respectively. The variables ω_x, ω_y, and ω_z are the Cartesian vorticity components in the x-, y-, and z-directions, respectively. We define a quantity $F_y \equiv \langle I_0 \cdot I_y \cdot |\lambda_2| \rangle$ to denote the occurrence of the spanwise vortex via the head portion of the reversed horseshoe vortical structure. Here $\langle \cdot \rangle$ denotes the phase averaging. In calculating F_y, we weigh the quantity by the magnitude of λ_2 to highlight strong vortices. Similarly, we use $F_x \equiv \langle I_0 \cdot I_x \cdot |\lambda_2| \rangle$ to denote quasistreamwise vortices that are mainly horizontal, and $F_z \equiv \langle I_0 \cdot I_z \cdot |\lambda_2| \rangle$ for vortices that have a large vertical component.

Figure 8(a)(i) shows the contours of F_x for the case of slow wave ($c/u_* = 2$). The high intensity region of F_x is located in a band between $[0.02\lambda, 0.2\lambda]$ above the wave surface, with the peak value above the windward face of the wave. This distribution indicates the concentration of quasistreamwise vortices above the windward face of the slow wave. Figure 8(b)(i) shows the contours of F_y. The high intensity region of F_y starts above the wave crest, extends downstream, and reaches its peak above the wave trough. Note that F_y denotes the occurrence of the spanwise vortices, which correspond to the heads of the reversed horseshoe vortices in this case. The result in Fig. 8(b)(i) indicates that the reversed horseshoe vortices are concentrated above the wave trough. The distributions of quasistreamwise and reversed horseshoe vortices indicated, respectively, by F_x and F_y are consistent with the observation of the instantaneous flow field in Fig. 5.

As introduced earlier, the results shown in this paper are obtained from the simulation of flow over prescribed wave motion. To validate this approach, we have also performed air-water coupled simulations that directly capture the two-way interaction between the wind and the wave. As a result, the air flow features such as the turbulence intensity and the water flow features such as the shape of the wave evolve dynamically in the simulation, and the results are expected to be more physical.

For air-water coupled motion, two different simulation approaches have been used. In the first approach, the current DNS is coupled with wave simulation using a method called simulation of nonlinear ocean wave (SNOW),[40] which is based on the computationally efficient high-order spectral (HOS) method of Dommermuth and Yue.[41] A brief description of this DNS-SNOW coupled approach is given in Appendix A; the numerical details can be found in Refs. 42 and

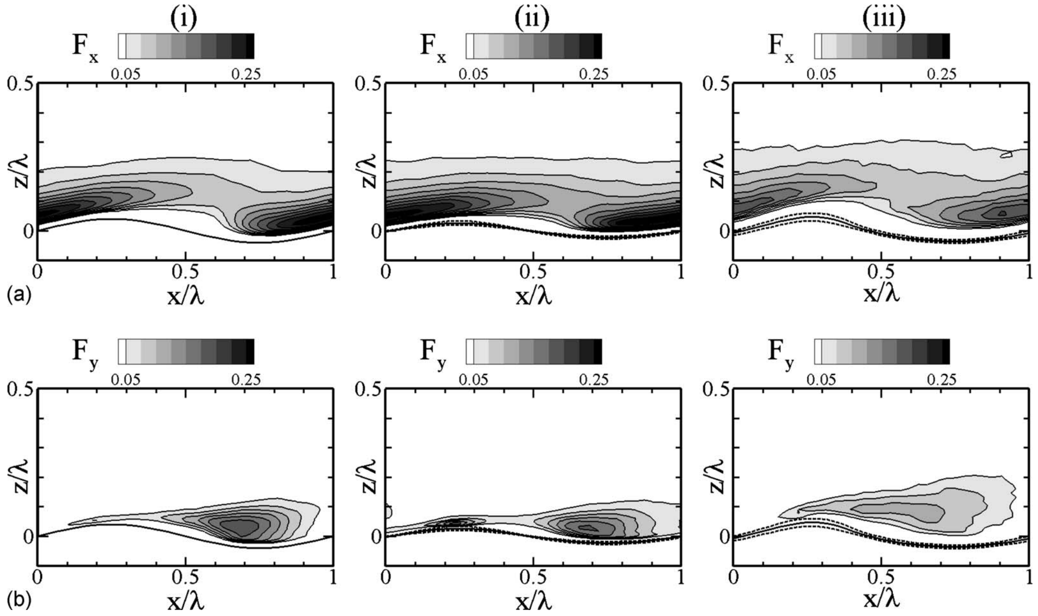

FIG. 8. Contours of (a) F_x and (b) F_y above the slow wave ($c/u_*=2$). Results are obtained from (i) current DNS, (ii) DNS-SNOW coupled simulation, and (iii) level-set simulation. The contour interval is 0.025. In (ii) and (iii), the mean surface elevation is denoted by the solid lines at the bottom of the plots, while the standard deviations of the surface are denoted by the dashed lines.

43. In the DNS- SNOW simulation, a fully developed turbulent flow over a water wave with $(ak,c/u_*)=(0.1,2)$ is used as the initial condition. The wave then evolves under wind pressure forcing. We take the sample data from $ak=0.12$ until $ak=0.27$ before the small-scale wave breaking (e.g., spilling breaking) happens (SNOW is a perturbation-based method and cannot describe wave breaking explicitly without modeling).

In the second approach, a level-set method (LSM) is used to simulate the turbulence-wave coupled flow, in which the air and water are treated together as one fluid system with varying density and viscosity and the flow interface is represented implicitly by a level-set function.[44] A brief description of the LSM is given in Appendix B. Similar to the DNS-SNOW simulation, the wave with the initial condition $(ak,c/u_*)=(0.1,2)$ grows in the simulation. We take the sample data from $ak=0.18$ until $ak=0.31$, which is steeper than the DNS-SNOW case. The surface wave is highly nonlinear with large steepness. Under strong wind forcing (small value of c/u_*), the shape of the steep water wave departs from the standard Stokes waveform and becomes asymmetric about the wave crest. The surface wave from our LSM simulation has an average skewness $S=\lambda_w/\lambda_l=1.21$, where λ_w and λ_l are horizontal lengths of $\overset{\frown}{P_1P_3}$ and $\overset{\frown}{P_3P_5}$ (Fig. 4), respectively. This skewness agrees well with the measurement of Chang *et al.*,[45] who reported a wind-forced steep water wave with a skewness of $S=1.25$.

As shown in Fig. 8, despite the difference in the waveform among wave simulations using the current DNS, DNS-SNOW, and LSM, the statistics of F_x and F_y are essentially the same among the three approaches. The difference is quantitative rather than qualitative, and the indication for the quasistreamwise vortices and horseshoe heads is obvious and consistent for all the three approaches. For LSM, we have also tested different Weber numbers so that the capillary wave appears at different scales (in Fig. 8, the surface fluctuations are denoted by the dashed lines) and found that the difference in the coherent vortical structures is negligibly small (comparison not shown due to space limitation). The insensitivity of the coherent vortices to the surface details suggests that the vortices are mainly affected by the outer flow structure, as illustrated in Fig. 4 (more results on the streamline pattern for the slow wave case will be given in Fig. 15). The motion of the outer flow relative to the waveform is dominated by the wave age. Therefore, the wave age is the most important parameter governing the characteristics of coherent vortices in turbulence over progressive waves.

B. Conditional sampling based on QDs of turbulence motion

Previous research of flat wall bounded turbulence indicated that the near-wall coherent vortical structures are often related to the turbulence motions of ejection and sweep (see, e.g., Ref. 24). Several conditional sampling methods have been developed to educe the vortical structures associated with the turbulence motions. Examples include the variable-interval time-averaging method,[46] the variable-interval space-averaging (VISA) method,[22] the quadrant (QD) method,[47] and the linear stochastic estimation method.[48] In our study, we have used the VISA and QD methods to educe the vortical structures above the wave surface and to illustrate the relationship between vortical structures and momentum transport. Good agreement between these two approaches has been obtained. In this paper, we present only the QD results without losing generality.

The contribution to the Reynolds stress $\langle -u'w' \rangle$ can be divided into four QDs: Q1 $(u'>0,w'>0)$, Q2 $(u'<0,w'$

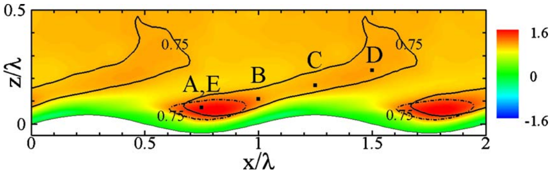

FIG. 9. (Color online) Contours of the normalized Reynolds stress $\langle -u'w'\rangle/u_*^2$ over the slow wave ($c/u_*=2$). High intensity regions of $\langle -u'w'\rangle_2/u_*^2$ and $\langle -u'w'\rangle_4/u_*^2$ are denoted by the 0.75 contour with solid and dash-dot lines, respectively. Points A ($x/\lambda=0.75$, $z/\lambda=0.07$), B ($x/\lambda=1.00$, $z/\lambda=0.10$), C ($x/\lambda=1.25$, $z/\lambda=0.16$), and C ($x/\lambda=1.50$, $z/\lambda=0.21$) are the detection positions for the QD-2 method; point E ($x/\lambda=0.75$, $z/\lambda=0.06$) is the detection position for the QD-4 method.

>0), Q3 ($u'<0, w'<0$), and Q4 ($u'>0, w'<0$). Hereinafter, the contribution to the total Reynolds stress from the mth-QD is referred to as $\langle -u'w'\rangle_m$; the QD conditional averaging method for detecting the mth-QD related structures is referred to as the QD-m method. Taken QD-2 method as an example, the detection function is defined as[47]

$$D(y,t;x,z) = \begin{cases} 1 & \text{if } u'<0,\ w'>0 \ \text{ and } \ u'w'/\langle u'w'\rangle > \beta, \\ 0 & \text{otherwise,} \end{cases} \tag{10}$$

where β is a positive threshold that controls the intensity of the Q2 events to be detected.

As shown by previous studies,[16,17,19,21] the distribution of $\langle -u'w'\rangle$ has a strong dependence on the wave phase, and this dependence varies significantly as the wave age changes. Figure 9 shows the color contours of the total Reynolds stress above the slow wave ($c/u_*=2$). Similar to the flat wall case,[34] the majority of the contribution to the total Reynolds stress $\langle -u'w'\rangle$ comes from the Q2 (ejection) and Q4 (sweep) events. As shown in Fig. 9, the high intensity regions of $\langle -u'w'\rangle_2$ and $\langle -u'w'\rangle_4$ are located above the windward face and the wave trough, which are indicated by solid and dash-dot lines, respectively. The contribution from the Q1 and Q3 events is negligible and is not shown here. Based on the distribution of Reynolds stress, we choose the representative detection positions A–D for QD-2 method and E for QD-4 method, which are marked in Fig. 9. The threshold in Eq. (10) is chosen to be $\beta=2$.

Figure 10(a) shows the conditionally averaged turbulence structure associated with the Q2 events around the detection position B. As shown, two counter-rotating quasistreamwise vortices exist in the conditionally averaged flow field. When observed along the $+x$-direction, the vortex on the left side has a streamwise vorticity component $\omega_x<0$, and the vortex on the right side has a streamwise vorticity $\omega_x>0$. It is apparent that the counter-rotating vortex pair induce an upwelling motion (ejection) between them, which results in high value of $-u'w'$ there.

To check the sensitivity of the conditionally averaged result to the sampling criterion β, we repeat the above conditional average calculation with $\beta=0.5$, 1, 4, and 8 and obtained consistent characteristics of the vortical structure, with only the intensity of the structure slightly changed. This result is consistent with a similar validation in Ref. 47 and confirms that the result we obtained with $\beta=2$ is representative.

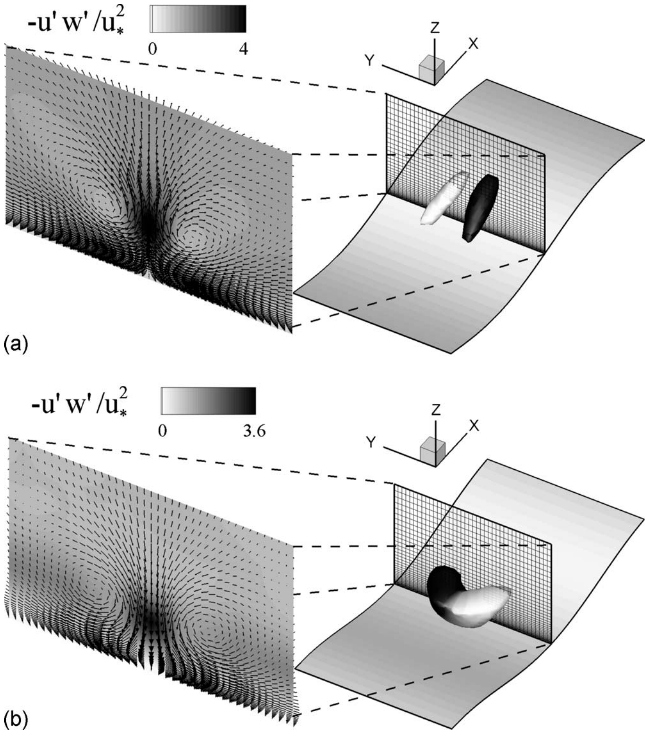

FIG. 10. Educed coherent structure by QD conditional sampling method with (a) QD-2 detection at location B [Fig. 9] and (b) QD-4 detection at location E (Fig. 9). The detection threshold is $\beta=2$. The vortical structures are represented by the isosurface of $\lambda_2=-0.1$. The structure with $\omega_x>0$ are marked by the dark color; the structure with $\omega_x<0$ are marked by the light color. The contours of the normalized turbulent momentum flux $-u'w'/u_*^2$ and the fluctuation velocity vectors (v',w') are shown on the (y,z)-plane crossing the detection point.

Figure 10(b) shows the conditionally averaged reversed horseshoe vortical structure associated with the Q4 events around the detection position E. The downwelling motion (sweep) associated with its head and two counter-rotating legs generates large turbulent momentum flux $-u'w'$. The result we obtained here is consistent with Kim and Moin;[47] they studied a turbulent channel flow and showed that the reversed horseshoe vortices are associated with the sweep event.

In order to study the dependence of these QD-associated vortical structures on the wave phase, we compile the results from the detection positions A–E and plot them together in Fig. 11. In order to describe the spatial feature of these vortical structures, we define two angles: α is the angle between the x-axis and the projection of the vortical structure in the (x,y)-plane (hereinafter is referred to as the tilting angle); and φ is angle between the x-axis and the projection of the vortical structure in the (x,z)-plane (hereinafter is referred to as the inclination angle). The values of the tilting and inclination angles of structures in Fig. 11 are listed in Table II. It should be noted that although the size of the vortical structure varies when different values of λ_2 are used, the essential

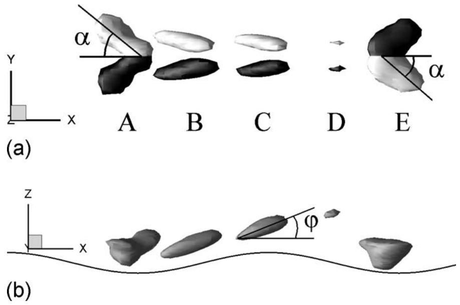

FIG. 11. Educed vortical structures above the slow wave ($c/u_*=2$): (a) top view and (b) side view. Structures A–E are educed by detectors at locations A–E in Fig. 9, respectively. The vortical structures are represented by the isosurface of $\lambda_2=-0.071$. The structures with $\omega_x>0$ are marked by the dark color; the structures with $\omega_x<0$ are marked by the light color.

geometry of the vortical structure is not sensitive to λ_2. In Fig. 11, to compare the sizes among different vortical structures, we use a fixed value of λ_2 for them.

As shown in Fig. 11, above the wave trough (position A), the Q2 event is associated with a horseshoelike vortex with the head downstream and the legs upstream; while above the windward face (position B), wave crest (position C), and the leeward face (position D), the vortical structures change to counter-rotating vortex pairs. Interestingly, the result shows that above the windward face, the tilting angle α decreases as the streamwise position moves downstream (Table II). The result also indicates that the size of the vortical structure reduces significantly above the leeward face compared to above the windward face. The Q4 event above the wave trough (position E) is associated with a reversed horseshoe vortex with the head on the upstream side. Due to the bulky geometry of structure E, its inclination angle is difficult to specify.

We also note that the direct observation from the instantaneous flow field (Fig. 5) indicates that the quasistreamwise vortices often appear individually. In the conditionally averaged field, the paring of quasistreamwise vortices is an artifact of the conditional averaging method and is as expected (see, e.g., Ref. 49). Nevertheless, the vortical structures educed by the QD method provide useful information such as the wave phase dependence of the coherent vortical structures above the surface wave. To obtain more accurate result on the geometry of the vortical structures, we investigate in Sec. III C direct extraction of the characteristic vortices for conditional sampling.

C. Direct sampling of characteristic vortical structures

Instead of educing the coherent vortical structures by detecting other related physical quantities such as the Reynolds stress and the QDs, we can obtain the vortical structure samples directly based on the geometric characteristics of the vortices. Details of the direct sampling procedure are given in Appendix C.

After the samples are obtained, we interpolate these sample fields from the boundary-fitted grid system to a Cartesian grid system. The sample fields are then shifted horizontally so that the points of the maximum $|\omega_x|$ in the structure are located at the horizontal center of each sampling window. We then calculate the ensemble average of the sample fields. We remark that both the velocity and the wave surface elevation of the sample fields are averaged. The ensemble-averaged flow field provides the details of the vortical structure, while the ensemble-averaged surface elevation illustrates the spatial relationship between the coherent vortical structures and the underlying surface wave.

Figures 12(a) and 12(b) show the ensemble-averaged quasistreamwise vortex above the slow wave ($c/u_*=2$) obtained from this direct sampling method. The averaged quasistreamwise vortices are located above the windward face [$\widetilde{P_1P_3}$ in Fig. 4(a)] of the wave, consistent with the result in Fig. 8. Hereinafter, a quasistreamwise vortex with positive ω_x is referred to as QSP, while a quasistreamwise vortex with negative ω_x is referred to as QSN. When observed along the $+x$-direction, the vortex QSN inclines to the $-y$-direction as shown in Fig. 12(b) (the vortex QSP inclines to the $+y$-direction; result not shown). This is consistent with the result of the QD method in Fig. 11. The bending tail of the vortex is smeared out during the averaging process because of the variation in the bending direction.

In the averaged field, no quasistreamwise vortex with an opposite sign of ω_x is observed near the primary vortex. This result is consistent with the observation of the instantaneous flow field (Fig. 5) that the quasistreamwise vortices above the surface waves usually appear individually rather than in pairs.

The ensemble-averaged result of the reversed horseshoe vortex is shown in Figs. 12(c) and 12(d). The head of the reversed horseshoe is captured clearly. Due to the large variation in the tilting and inclination angles of the legs, the tails of the two legs are smeared out. The ensemble-averaged surface elevation indicates that the reversed horseshoe vortex

TABLE II. Tilting and inclination angles of structures in Fig. 11.

	Q2				Q4
Vortical structure	A	B	C	D	E
α	31.5°	13.5°	9.5°	13.5°	36°
φ	25.5°	20.5°	21.5°	24°	

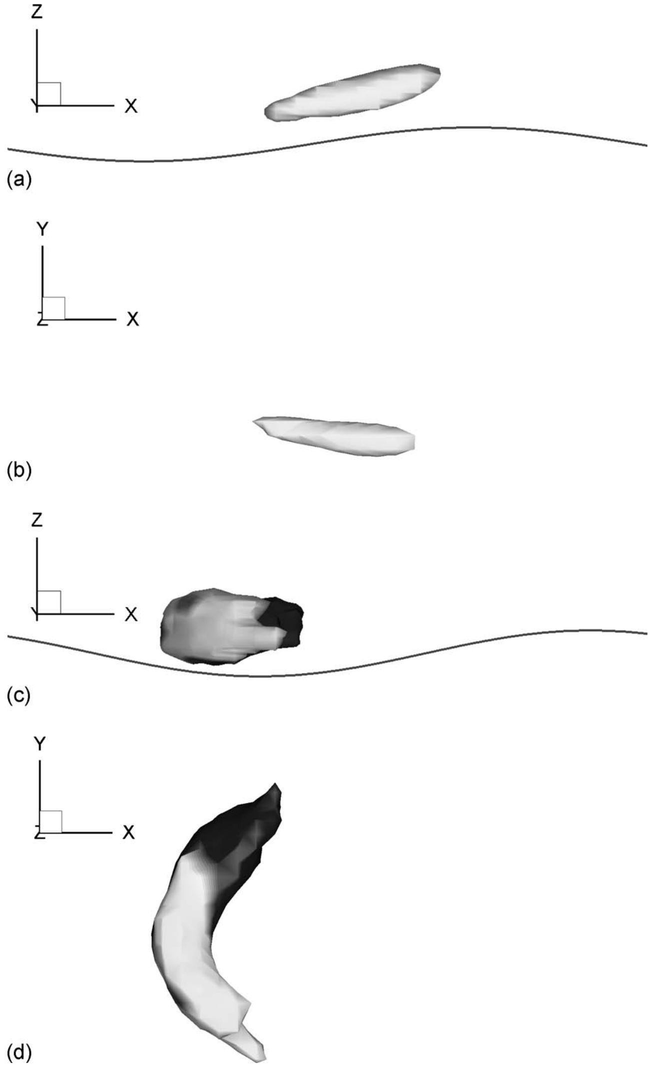

FIG. 12. Ensemble-averaged vortical structures from the extracted samples for the case of slow wave ($c/u_*=2$): (a) side view and (b) top view of quasistreamwise vortex with $\omega_x<0$; (c) side view and (d) top view of reversed horseshoe vortex. The structures with $\omega_x>0$ are marked by the dark color; those with $\omega_x<0$ are marked by the light color.

is located above the wave trough, with its head upstream of the trough. This spatial relationship is consistent with the result in Fig. 11.

Since the criterion of the above direct sampling method is based on the spatial features (i.e., geometry and primary direction) of the vortical structure, the educed vortical structures by this method resemble the instantaneous ones more than those educed by the QD method do. The results from the above direct sampling method confirm the existence and characteristics of the reversed horseshoe vortices above the wave trough and the quasistreamwise vortices above the windward face, which are found to be associated with the turbulent momentum flux by the QD-*m* method. The direct sampling result also indicates that the quasistreamwise vortices often appear individually, which is consistent with the direct observation of the instantaneous flow field.

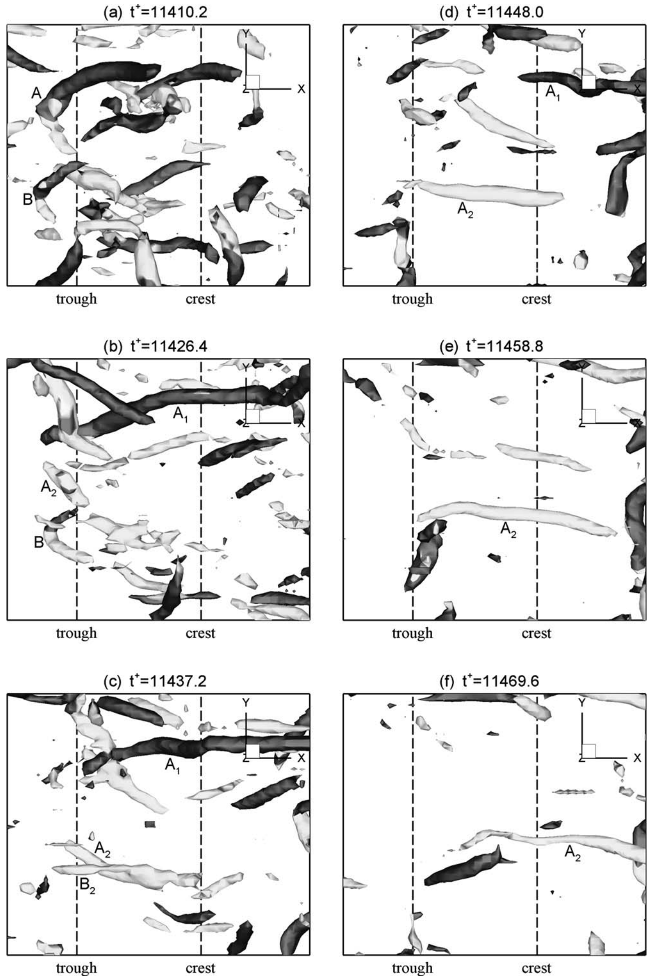

FIG. 13. History of vortex evolution above the slow wave ($c/u_*=2$). The flow field is observed from above in the wave-following frame. The vortical structures are identified by the isosurface of $\lambda_2=-1.2$. The structures with $\omega_x>0$ are marked by the dark color; the structures with $\omega_x<0$ are marked by the light color. The positions of the wave trough and crest are indicated by the dashed lines.

D. Evolution of vortical structures over the slow wave

The results in Secs. III B and III C indicate that different types of vortical structures exist at different streamwise locations with respect to the waveform. In this section we investigate their evolution and reveal the transformation among them.

We first examine the instantaneous vortex fields at successive times. Figure 13 shows the history of vortex evolution above the slow wave ($c/u_*=2$). As discussed in Sec. II, in the slow wave case, the vortices propagate from left to right in the wave-following frame [Fig. 4(a)].

At $t^+=11\,410.2$ [Fig. 13(a)], the reversed horseshoe vortices A and B are located above the wave trough, with their heads slightly upstream of the wave trough. At $t^+=11\,426.4$ [Fig. 13(b)], vortex A breaks at its head and the two legs becomes QSP A_1 and QSN A_2. The QSP A_1 is then further turned to the streamwise direction above the trough, stretched along the streamwise direction above the windward face, and extended over the wave crest [Fig. 13(c)]. Meanwhile, the QSP leg of the reversed horseshoe vortex B disappears and its QSN leg B_2 merges into the QSN A_2, which is then turned to and stretched along the streamwise direction as well [Figs. 13(c)–13(e)]. As the quasistreamwise vortices A_1 and A_2 propagate over the wave crest, they lose their intensity above the leeward face of the wave crest and above the next wave trough [Figs. 13(e) and 13(f)].

The result in Fig. 13 indicates that there exist transformations from the reversed horseshoe vortices to the quasistreamwise vortices due to the vortex turning from spanwise direction to streamwise direction above the wave trough and the streamwise vortex stretching above the windward face of the wave. These transformations are found to be universal above the slow wave and they are responsible for the formation of the majority of the quasistreamwise vortices. This evolution also provides an explanation for the vortices distribution educed by the QD method (Fig. 11). The variation in the tilting angle α in Fig. 11 can be regarded as a consequence of this transformation process.

The above investigation of vortex evolution history indicates that vortex turning and stretching play an important role in the formation of the quasistreamwise vortices. We now study the vorticity dynamic equation to quantitatively investigate the effect of vortex turning and stretching in the vortex evolution process. The phase-averaged dynamic equations for vorticity components ω_x and ω_z are (e.g., Ref. 50)

$$\frac{D\langle\omega_x\rangle^{1p}}{Dt} = \underbrace{\left\langle \omega_x \frac{\partial u}{\partial x}\right\rangle^{1p}}_{\mathcal{T}_1^1} + \underbrace{\langle\omega_y\rangle\left\langle\frac{\partial u}{\partial y}\right\rangle^{1p}}_{\mathcal{T}_{2m}^1} + \underbrace{\left\langle \omega_y' \frac{\partial u}{\partial y}\right\rangle^{1p}}_{\mathcal{T}_{2t}^1} + \underbrace{\left\langle \omega_z \frac{\partial u}{\partial z}\right\rangle^{1p}}_{\mathcal{T}_3^1} + \underbrace{\frac{1}{\mathrm{Re}}\langle\nabla^2\omega_x\rangle^{1p}}_{\mathcal{D}^1}, \tag{11}$$

$$\frac{D\langle\omega_z\rangle^{3p}}{Dt} = \underbrace{\left\langle \omega_x \frac{\partial w}{\partial x}\right\rangle^{3p}}_{\mathcal{T}_1^3} + \underbrace{\langle\omega_y\rangle\left\langle\frac{\partial w}{\partial y}\right\rangle^{3p}}_{\mathcal{T}_{2m}^3} + \underbrace{\left\langle \omega_y' \frac{\partial w}{\partial y}\right\rangle^{3p}}_{\mathcal{T}_{2t}^3} + \underbrace{\left\langle \omega_z \frac{\partial w}{\partial z}\right\rangle^{1p}}_{\mathcal{T}_3^3} + \underbrace{\frac{1}{\mathrm{Re}}\langle\nabla^2\omega_z\rangle^{3p}}_{\mathcal{D}^3}. \tag{12}$$

Here, D/Dt is the material derivative, $\mathcal{T}_1^1$ and $\mathcal{T}_3^3$ are the vortex stretching of ω_x and ω_z, respectively, $\mathcal{T}_j^i (i \neq j)$ is the vortex turning from ω_j to ω_i, and $\mathcal{D}^i$ is the viscous diffusion of ω_i. The turning term associated with ω_y is further decomposed into the contributions from $\langle\omega_y\rangle$ and ω_y', which are denoted by the subscripts m and t, respectively. The operator $\langle f\rangle^{ip}$ denotes the phase average of f with the condition $\omega_i > 0$ [the problem is antisymmetric between $\omega_i>0$ and $\omega_i<0$; if we do averaging for both, the terms in Eqs. (11) and (12) will be zero].

In this subsection, we focus on the dynamic equation of ω_x to study the evolution of the quasistreamwise vortices.

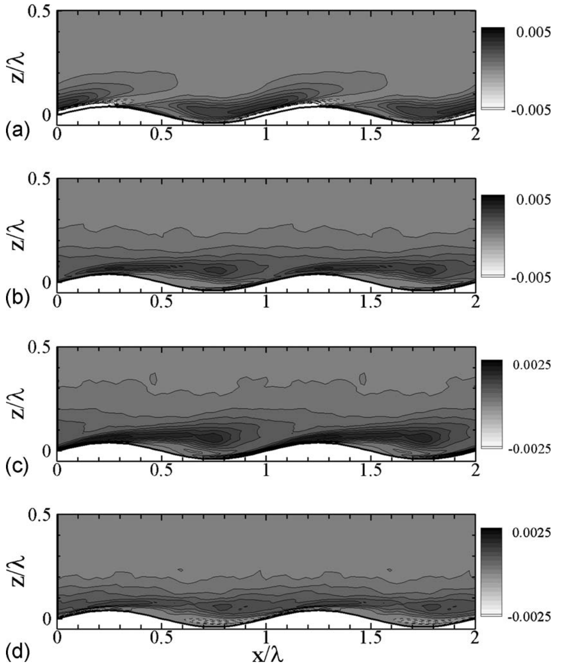

FIG. 14. Contours of the vortex stretching and turning terms for the positive streamwise vorticity above the slow wave ($c/u_*=2$) normalized by $(u_*^2/\nu)^2$: (a) vortex stretching of ω_x, $\mathcal{T}_1^1=\langle\omega_x(\partial u/\partial x)\rangle^{1p}$; (b) vortex turning from the spanwise vorticity fluctuation ω_y' to ω_x, $\mathcal{T}_{2t}^1=\langle\omega_y'(\partial u/\partial y)\rangle^{1p}$; (c) vortex turning from ω_y' to ω_x by the strain field S_{12}, $\mathcal{T}_{2t}^1|_{\text{strain}}=\langle\omega_y' S_{12}\rangle^{1p}$; and (d) vortex turning from ω_y' to ω_x by the rotation field Ω_{12}, $\mathcal{T}_{2t}^1|_{\text{rotation}}=\langle\omega_y'\Omega_{12}\rangle^{1p}$. The dashed contour lines represent negative values.

Among the terms in Eq. (11), $\mathcal{T}_1^1$ and $\mathcal{T}_{2t}^1$ are found to be dominant. Here, $\mathcal{T}_1^1$ represents the vortex stretching of the quasistreamwise vortices and $\mathcal{T}_{2t}^1$ represents the vortex turning from the spanwise vortices (i.e., the heads of the reversed horseshoe vortices) to the streamwise vortices.

We note that in some literature (e.g., Ref. 50), $\mathcal{T}_j^i$ is used to study vortex stretching and turning mechanism; while in some others (e.g., Ref. 36), this term is further decomposed into

$$\underbrace{\left\langle \omega_j \frac{\partial u_i}{\partial x_j}\right\rangle^{ip}}_{\mathcal{T}_j^i} = \underbrace{\langle\omega_j S_{ij}\rangle^{ip}}_{\mathcal{T}_j^i|_{\text{strain}}} + \underbrace{\langle\omega_j \Omega_{ij}\rangle^{ip}}_{\mathcal{T}_j^i|_{\text{rotation}}}, \tag{13}$$

where $S_{ij}=0.5(\partial u_i/\partial x_j+\partial u_j/\partial x_i)$ and $\Omega_{ij}=0.5(\partial u_i/\partial x_j-\partial u_j/\partial x_i)$ are the symmetric (strain rate) and antisymmetric (rotation rate) parts of the velocity gradient tensor, respectively. Here, the terms $\mathcal{T}_j^i|_{\text{strain}}$ are the vortex stretching (when $i=j$) and turning (when $i\neq j$) by the strain rate; the terms $\mathcal{T}_j^i|_{\text{rotation}}$ are the vortex turning by the rotation rate. We note that the stretching terms satisfy $\mathcal{T}_1^1=\mathcal{T}_1^1|_{\text{strain}}$ and $\mathcal{T}_3^3=\mathcal{T}_3^3|_{\text{strain}}$; we also note that due to $\omega_x\Omega_{i1}+\omega_y\Omega_{i2}+\omega_z\Omega_{i3}=0$, the total contributions to vortex dynamics due to Ω_{ij} from $j=1$, 2, and 3, $\Sigma_{j=1}^3\mathcal{T}_j^i|_{\text{rotation}}$, is zero.

As shown in Fig. 14(a), the high intensity region of $\mathcal{T}_1^1$ is located above the windward face of the wave, where the quasistreamwise vortices concentrate [Figs. 8(a) and 11]. Above the slope downstream of the wave crest, the intensity

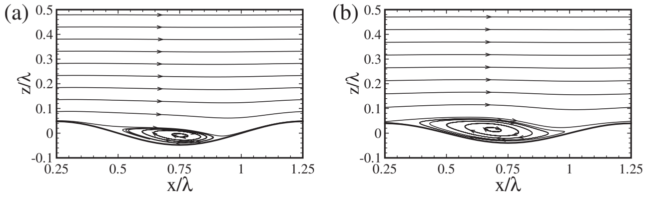

FIG. 15. Streamline patterns over (a) stationary wavy wall and (b) slow water wave. In (b), the streamlines are calculated in the wave-following frame.

of the vortex stretching reduces significantly; without the support of vortex stretching, the quasistreamwise vortices are dissipated there, which has been indicated by the low value of F_x in Fig. 8(a) and the relatively smaller size of vortex D in Fig. 11.

Figure 14(b) shows that the high intensity region of the vortex turning term $\mathcal{T}^1_{2t}$ is located above the wave trough. This location is consistent with the concentration region of the reversed horseshoe vortices [Figs. 8(b) and 12(c)]. The above coincidence indicates that there exists transformation from the reversed horseshoe vortices to the quasistreamwise vortices above the wave trough. For the slow wave case, the magnitude of $\partial v/\partial x$ is smaller than that of $\partial u/\partial y$. Therefore, the distributions of $\mathcal{T}^1_{2t}|_{\text{strain}}$ [Fig. 14(c)] and $\mathcal{T}^1_{2t}|_{\text{rotation}}$ [Fig. 14(d)] are similar to the distribution of $\mathcal{T}^1_{2t}$ [Fig. 14(b)], with the magnitudes multiplied by the 0.5 factor. The consistency between the mechanisms indicated by $\mathcal{T}^1_{2t}$ and $\mathcal{T}^1_{2t}|_{\text{strain}}$ shows that the above analysis is valid for both definitions of vortex turning. The distributions of vortex stretching and turning shown in Fig. 14 are consistent with the evolution history of the vortical structures shown in Fig. 13.

Finally, we note that the formation of quasistreamwise vortices over a stationary wavy wall was investigated in literature. Calhoun and Street[6] calculated the Görtler number in a turbulent flow over a stationary wavy wall and showed that the flow is unstable above the windward face of the wave. Tseng and Ferziger[7] examined instantaneous vorticity field in successive times, and showed the breakdown and reconnection of quasistreamwise vortices. Phillips *et al.*[51] performed a stability analysis and found that the Craik–Leibovich CL2-$O(1)$ instability[52,53] mechanism leads to the formation of quasistreamwise vortices above the stationary wavy wall. In the present slow wave case, although the turbulence above the wave is different from that above a stationary wavy wall because of the boundary motion of the wave, there are still some similarities in the streamline patterns.[21] As shown in Fig. 15, for both the slow and stationary wave cases, there exists a circulation zone right above the wave trough, and the outer flow streamlines leave the wave surface and stride over the circulation zone. The size of the circulation zone in the slow wave case is larger than that in the stationary wave case. Above the windward face, in both cases the outer flow streamlines reapproach the wave surface and have a concave curvature. As shown by Calhoun and Street,[6] this concave streamline curvature is critical for the generation of flow instability and the formation of quasistreamwise vortices in the stationary wavy wall case. Similar instability mechanism is expected for the slow wave case due to the similar concave streamline pattern above the windward face. In addition to this direct formation of streamwise vortices due to the instabilities, however, in this study we found that the transformation of reversed horseshoe vortices to quasistreamwise vortices is significant. This new finding may add another possible mechanism for the explanation of quasistreamwise vortex formation over wavy surfaces.

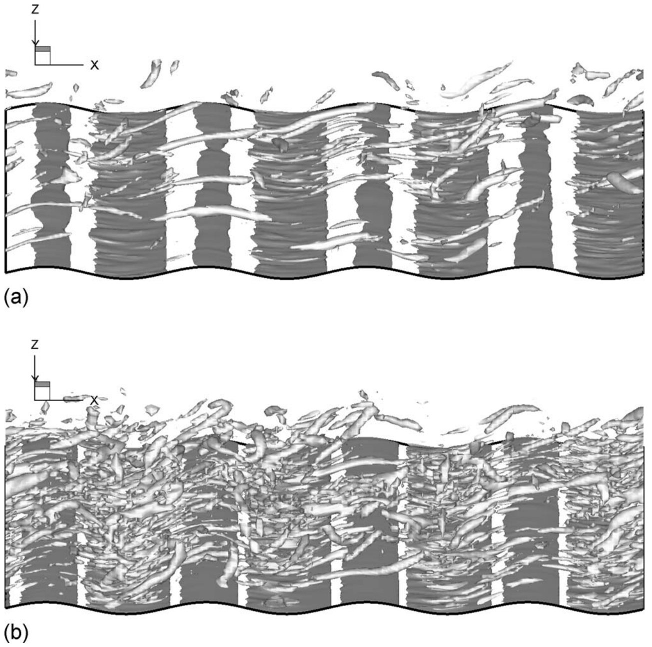

FIG. 16. Snapshots of near-surface coherent vortical structures in the turbulence fields over the (a) intermediate wave $(c/u_*=14)$ and (b) fast wave $(c/u_*=25)$. The vortical structures are identified by the isosurface of $\lambda_2=-1.0$. The gray color on the wave crests and troughs corresponds to large spanwise vortex sheets.

IV. COHERENT VORTICAL STRUCTURES ABOVE THE INTERMEDIATE AND FAST WAVES

In this section, we study the coherent vortical structures above the intermediate $(c/u_*=14)$ and fast $(c/u_*=25)$ waves. Figures 16(a) and 16(b) show the instantaneous vortices above the intermediate and fast waves, respectively. We note that there exist large spanwise vortex sheets on the wave crests and troughs. These vortex sheets are caused by the strong action of the wave orbital motion [measured by akc in Eq. (4)] on the turbulent flow. In the case of slow wave $(c/u_*=2)$, the vortex sheet is not observed because the wave motion is relatively slow. Figure 16 shows that for both the intermediate and fast waves, quasistreamwise vortices are the dominant vortical structure above the wave surface. The spatial frequency of the occurrence of the quasistreamwise vortices in the case of $c/u_*=14$ is lower than that in the case of $c/u_*=25$. Over the wave crest and the slope upstream of the wave crest, the vortices bend to follow the local curvature of the wave surface. Above the slope downstream of the wave trough, the vortices incline vertically to have large vertical parts. Figure 4(b) shows a sketch of the characteristic vortices for the intermediate wave case. We note that different from the slow wave case, in the wave-following frame, the vortices travel in the $-x$-direction.

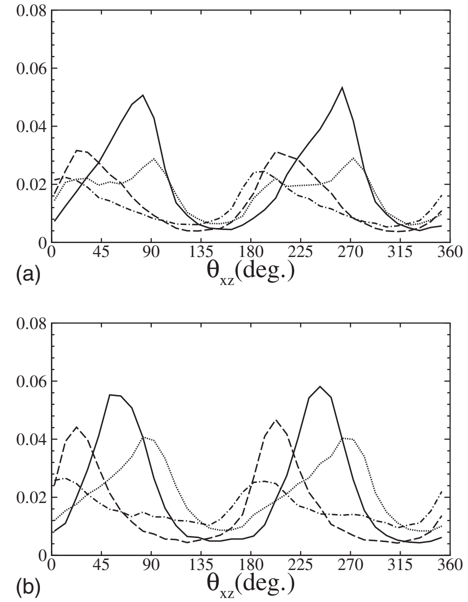

FIG. 17. Probabilities of two-dimensional vorticity angle θ_{xz} (the angle from the $+x$-axis to the vorticity $\omega_x\mathbf{i}+\omega_z\mathbf{k}$) at four streamwise locations above the (a) intermediate wave ($c/u_*=14$) and (b) fast wave ($c/u_*=25$): —, windward face; – – –, crest; –·–, leeward face; and ····, trough. The vertical locations are chosen to be the locations of peak F_x and F_z, as shown in Fig. 18.

In Secs. IV A–IV D, we follow the same procedure as in the slow wave case to analyze the different aspects of the characteristics of the quasistreamwise vortices for the intermediate and fast wave cases.

A. Statistics of vortical structures above the intermediate and fast waves

We first study the two-dimensional vorticity inclination angle θ_{xz} (defined in Fig. 6) in a way similar to that in the slow wave case. Figure 17(a) shows the probability of θ_{xz} above the leeward face, crest, windward face, and trough for the intermediate wave case ($c/u_*=14$). Above the leeward face, θ_{xz} is concentrated around 10° and 190°. Above the wave crest, θ_{xz} is concentrated around 25° and 205°. Further upstream to above the windward face, θ_{xz} is concentrated around 85° and 265°, indicating the significance of the vertical vorticity component ω_z there. Above the wave trough, the distribution of θ_{xz} has a concentration around 90° and 270° and another concentration around 20° and 200°. The probability distribution in the fast wave case [Fig. 17(b)] is similar to that in the intermediate wave case.

Next, we use the conditionally averaged quantities F_x and F_z (defined in Sec. III A) to measure the spatial frequency of the occurrence of streamwise and vertical vortices, respectively. Figure 18 shows the contours of F_x and F_z for the cases of $c/u_*=14$ and 25. In both cases, the high intensity regions of F_x and F_z are located above the wave crest and windward face, respectively. The difference in the locations of the peak regions between F_x and F_z indicates that the vortices are horizontal above the crest, but incline to the vertical direction over the windward face of the wave. We also find that the magnitudes of F_x and F_z in the case of $c/u_*=25$ are larger than those in the case of $c/u_*=14$, which indicates the higher spatial frequency of vortices in the fast wave case (cf. Fig. 16). Despite the difference in the spatial frequency, the results in Figs. 17 and 18 indicate that the essential features of the vortical structures in the intermediate and fast wave cases are very similar to each other. Due to space limitation, in subsequent subsections we present the intermediate wave results only.

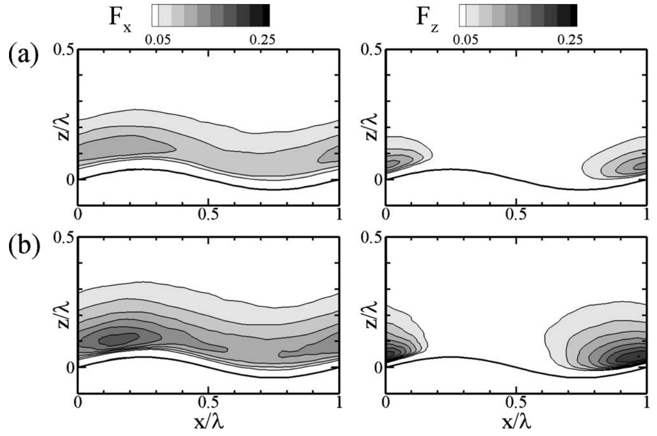

FIG. 18. Contours of F_x and F_z above the (a) intermediate ($c/u_*=14$) and (b) fast ($c/u_*=25$) waves. The contour interval is 0.025.

The above results indicate that as the near-surface flow propagates in the $-x$-direction in the wave-following frame, the projections of the vorticity vectors in the (x,z)-plane are almost horizontal above the leeward face and the crest, and then turn to the vertical direction above the windward face. The vortices further propagate to above the trough; meanwhile, new streamwise vortices are formed above the wave trough for the next wave period. The evolution of vortices will be studied in Sec. IV D.

It should be mentioned that in Fig. 16 (as well as in Fig. 5), the lower half of the computational domain is plotted. However, noticeable vortical structures are mainly located near the wave surface. This near surface concentration can also be seen from Fig. 18, which shows that the spatial frequency of the vortical structures reduces rapidly as the height becomes large. It should be pointed out that in the fast wave case, the critical layer height is too large to have significant effect on near surface events.[11] Figure 18 shows that vortical structures are rare above $z=\lambda/\pi$. Previous numerical studies, e.g., Refs. 13 and 16, showed that at $z>\lambda/\pi$, the effect of wave motion on turbulence vanishes. The domain heights in their studies are about one wavelength, $\bar{H}=\lambda$. In our simulations, an even larger value of $\bar{H}=2\lambda$ was used, which is sufficient to capture the essential vortex dynamics discussed in this paper.

B. Conditional sampling by the QD-*m* method

The distributions of the Reynolds stress $\langle -u'w'\rangle$ in the intermediate and fast wave cases are significantly different from that in the slow wave case (see, e.g., Refs. 16, 19, and 21). The Reynolds stress is negative above the windward face of the wave but positive above the leeward face.

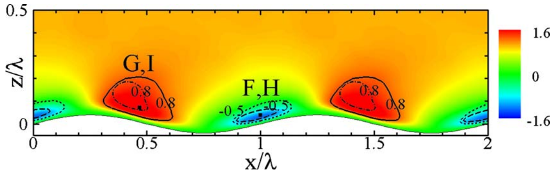

FIG. 19. (Color online) Contours of the normalized Reynolds stress $\langle -u'w'\rangle/u_*^2$ over the intermediate wave $(c/u_*=14)$. High intensity regions of $\langle -u'w'\rangle_1/u_*^2$ and $\langle -u'w'\rangle_3/u_*^2$ are denoted by the -0.5 contour with dotted and dashed contour lines, respectively; high intensity regions of $\langle -u'w'\rangle_2/u_*^2$ and $\langle -u'w'\rangle_4/u_*^2$ are denoted by the 0.8 contour with dash-dot and solid contour lines, respectively. The points F and H (both at $x/\lambda=1.00$, $z/\lambda=0.04$) denote the detection positions for the QD-1 and QD-3 methods, respectively; the points G and I (both at $x/\lambda=0.46$, $z/\lambda=0.05$) denote the detection positions for the QD-2 and QD-4 methods, respectively.

Figure 19 shows the distribution of the Reynolds stress above the intermediate wave $(c/u_*=14)$. The Q1 and Q3 events are responsible for the negative Reynolds stress above the windward face of the wave, and the Q2 and Q4 events are responsible for the positive Reynolds stress above the leeward face of the wave. In Fig. 19, the high intensity regions associated with Q1, Q2, Q3, and Q4 are indicated by dotted, dash-dot, dashed, and solid contour lines, respectively. Similar to the slow wave case, we apply the QD-m method to perform conditional averaging to educe vortical structures associated with each QD event. The detection positions F–I are marked in Fig. 19.

Figure 20(a) shows the conditionally averaged turbulence structure associated with the Q1 events around the detection position F. Note that there exist large spanwise structures right above the wave crest and trough (see Fig. 16). The existence of these vortex sheets reduces the visibility of the quasistreamwise structures associated with the QDs. The result in Fig. 20(a) indicates that the coherent vortical structures associated with the Q1 events consist of a pair of vortices. When observed along the $+x$-direction, the vortex on the left side has a vertical vorticity component $\omega_z>0$, and the vortex on the right side has $\omega_z<0$. They are almost parallel to each other. On both the (y,z) and (x,y)-planes crossing the detection point, the negative peak of $-u'w'$ is located between the two vortices. Unlike the velocity vectors in Fig. 10(a) for the slow wave case, the velocity vectors on the (y,z)-plane do not indicate obvious rotation motion. The velocity vectors on the (x,y)-plane clearly indicate a jet toward the $+x$-direction between the two vortices. The flow patterns on the (x,y)-plane and (y,z)-plane imply that the major fluid motion associated with the Q1 events is in the horizontal direction rather than in the vertical direction. This is because over the slope downstream of the wave trough, the vortices bend downward to have a significant vertical component, which induces horizontal momentum flux.

To confirm the above results, we plot the isosurfaces of the streamwise and spanwise vorticity components in Figs. 20(b) and 20(c), respectively. The isosurface of ω_x is located above the wave crest and the isosurface of ω_z is located above the windward face, both of which show a pair of counter-rotating vortices. The result in Fig. 20 indicates that the coherent vortical structures associated with the Q1 events are along the streamwise direction above the wave crest, and

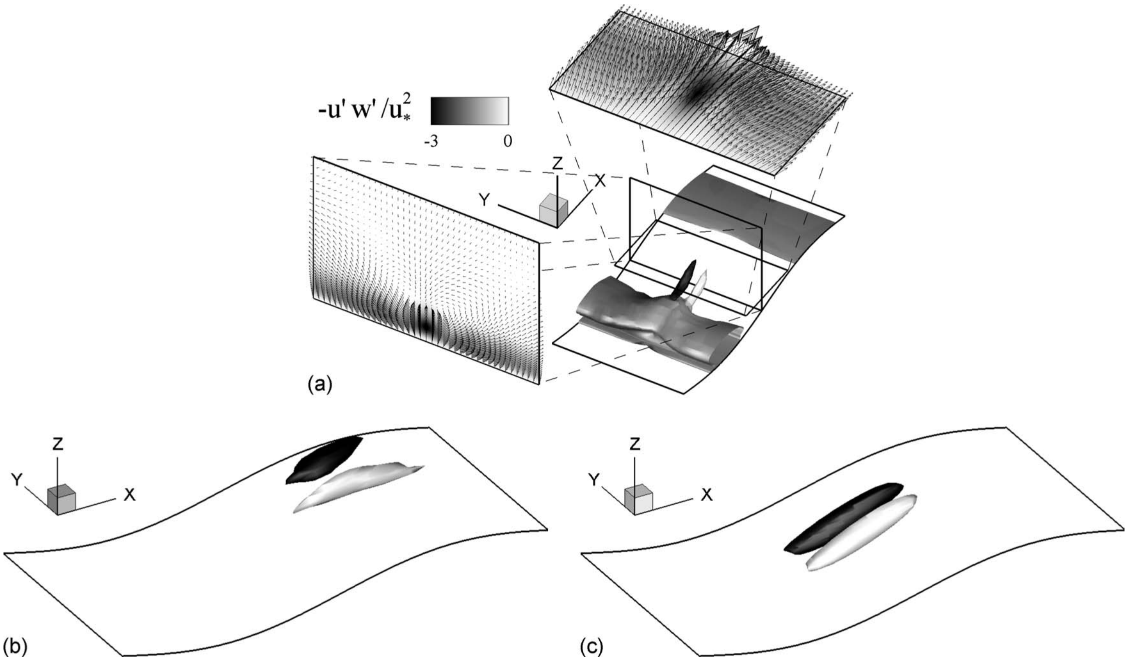

FIG. 20. Educed coherent structure by QD-1 conditional sampling with the detection position at location F in Fig. 19 and the threshold $\beta=2$. In (a), the vortical structures are represented by the isosurface of $\lambda_2=-0.033$. The structure with $\omega_z>0$ are marked by the dark color; the structure with $\omega_z<0$ are marked by the light color. The fluctuation velocity vectors (v',w') are shown on the (y,z)-plane crossing the detection point, and the fluctuation velocity vectors (u',v') are shown on the (x,y)-plane crossing the detection point. The contours of the normalized turbulent momentum flux $-u'w'/u_*^2$ are also shown on both planes. In (b) and (c), the structures in the same educed flow field are identified by the isosurfaces of $|\omega_x|=0.15$ and $|\omega_z|=0.5$, respectively. The structures with $\omega_i>0$ are marked by the dark color; the structures with $\omega_i<0$ are marked by the light color. For better view, in (b) the vortex sheets on the surface are removed.

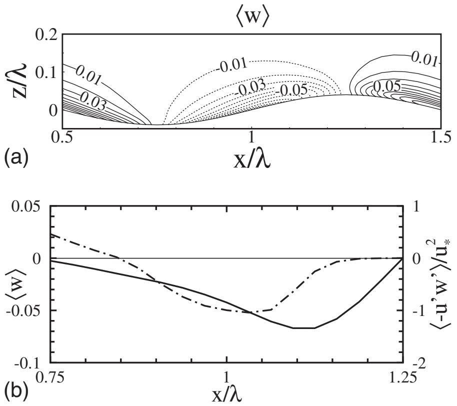

FIG. 21. Phase-averaged velocity field above the intermediate wave ($c/u_*=14$). In (a), the vertical velocity contours are plotted. Dashed contour lines represent negative values. The contour interval is 0.01. In (b), the local streamwise profiles of $\langle w\rangle$ (solid line) and $\langle -u'w'\rangle/u_*^2$ (dash-dot line) at the height $z/\lambda=0.04$ are plotted.

bend downward to the vertical direction when extending to the trough over the slope upstream of the wave crest [Fig. 4(b)].

We note that when the vortices bend downward, the magnitude of the vertical vorticity ω_z [Fig. 20(c)] is larger than that of the streamwise vorticity ω_x [Fig. 20(b)]. This is consistent with the result in Fig. 17, which shows that the vertical vorticity is significant above the windward face of the wave. The counter-rotating motion associated with the vertical vorticity induces a flux along the +*x*-direction. Due to the local streamwise profile of the vertical velocity $w(x)$ above the windward face of the wave as shown in Fig. 21, fluid particles with $u'>0$ carry negative vertical velocity to a downstream position where the negative vertical velocity is even larger in magnitude, resulting in $w'>0$. Similarly, $u'<0$ is associated with $w'<0$. Therefore, a region of $-u'w'<0$ is generated above the windward face of the wave.

Figure 22(a) shows the conditionally averaged turbulence structure associated with the Q2 events around the detection position G, which consists of a pair of counter-rotating quasistreamwise vortices. The vortex pair induces an upwelling motion and generates a high intensity region of Reynolds stress. This is similar to the ejection motion in the case of $c/u_*=2$ [Fig. 10(a)].

Figure 22(b) shows the conditionally averaged vortical structure associated with the Q3 events around the detection position H. The vortical structure is smeared out by the spanwise vortex sheet and is not clearly visible. We have also plotted the isosurfaces of $|\omega_x|=0.15$ and $|\omega_z|=0.5$ and found structure similar to the one in Figs. 20(b) and 20(c) (results not shown here due to space limitation). Figure 22(c) shows the conditionally averaged vortical structure associated with the Q4 events around the detection position I. The result clearly indicates a counter-rotating quasistreamwise vortex pair similar to that in Fig. 22(a), except that the positions of the positive and negative vortices are switched.

Similar to the discussion in Sec. III, the instantaneous vortices often appear individually rather than in pair, and the vortex pair shown in the plots of this subsection is an artifact of the QD conditional averaging method. In Sec. IV C, we investigate direct extraction of each individual vortical structure for conditional averaging.

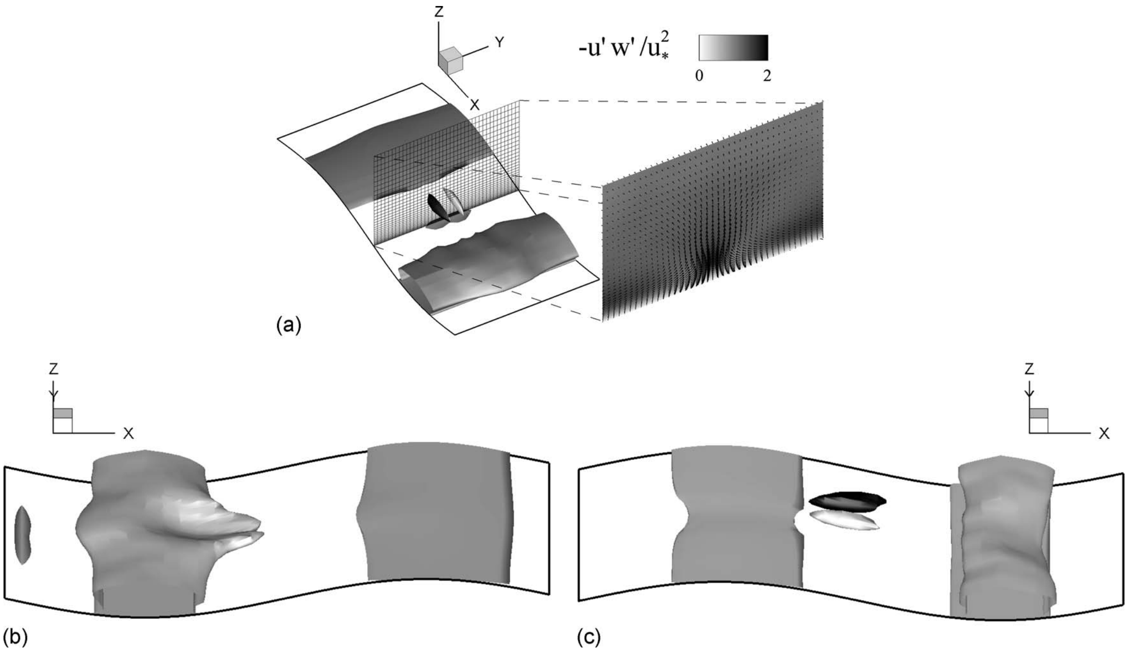

FIG. 22. Educed coherent structures by the QD method with: (a) QD-2 detection at location G (Fig. 19); (b) QD-3 detection at location H (Fig. 19); and (c) QD-4 detection at location I (Fig. 19). The detection criterion threshold is $\beta=2$. The vortical structures are represented by the isosurface of $\lambda_2=-0.08$. The structures with $\omega_x>0$ are marked by the dark color; the structures with $\omega_x<0$ are marked by the light color. In (a), the contours of the normalized turbulent momentum flux $-u'w'/u_*^2$ and the fluctuation velocity vectors (v',w') are shown on the (y,z)-plane crossing the detection point.

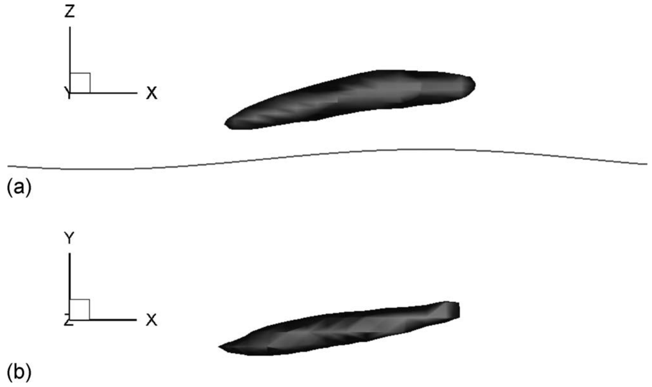

FIG. 23. Ensemble-averaged quasistreamwise vortex with $\omega_x>0$ from the extracted samples for the case of intermediate wave ($c/u_*=14$): (a) side view and (b) top view.

C. Direct sampling of characteristic vortical structures

In this subsection, we apply the direct sampling approach used in Sec. III C to the case of $c/u_*=14$. Recall that this approach requires the vortical structures to be isolated so that their shapes can be checked. Direct observation of the instantaneous flow field indicates that some quasistreamwise vortices are connected to the spanwise vortex sheet above the wave trough (see Fig. 16), which makes the extraction of vortices difficult there. As a result, in this study we check only the data points above the height of the vortex sheet. By doing this, we lose the information on the upstream ends of the vortices near the wave trough where they bend toward the vertical direction. The interaction between the vortices and the spanwise vortex sheet is beyond the scope of the present study and will be a subject of our future research.

Figure 23 shows the ensemble-averaged quasistreamwise vortices sampled by this direct sampling method. For better visualization, we removed the spanwise vortex sheets on the wave crest and trough when making the plot. Similar to the case of $c/u_*=2$, when observed along the $+x$-direction, the vortex QSP inclines slightly to the $+y$-direction as shown in Fig. 23(b), while the vortex QSN inclines slightly to the $-y$-direction (not shown due to space limitation). The vortices are almost straight in the horizontal plane. We note that the upstream end that has a significant vertical component is smeared out during the averaging process because of the termination in sampling when the wave trough is approached and because of the variation in the vertical bending for different vortices. The ensemble-averaged surface elevation indicates that the quasistreamwise vortices are located above the wave crest and the slope upstream of the crest. When observed from the side, the vortices bend in the vertical plane to follow the curvature of the wave surface. This change in the primary direction is consistent with the result in Figs. 18 and 20.

Direct sampling of quasistreamwise vortices indicate that the vortices QSP and QSN in the case of $c/u_*=14$ are more likely to appear individually rather than in pair. This is consistent with the case of $c/u_*=2$. As shown in Sec. IV B, the QD-m method captures features of the upstream and downstream ends of the quasistreamwise vortices on the upstream and downstream slopes of the wave crest, respectively. The direct sampling method in this subsection, on the other hand, provides information on the quasistreamwise vortices above the wave crest. These two methods complement each other. The combined results provide a more complete picture of the characteristics of the coherent vortical structures.

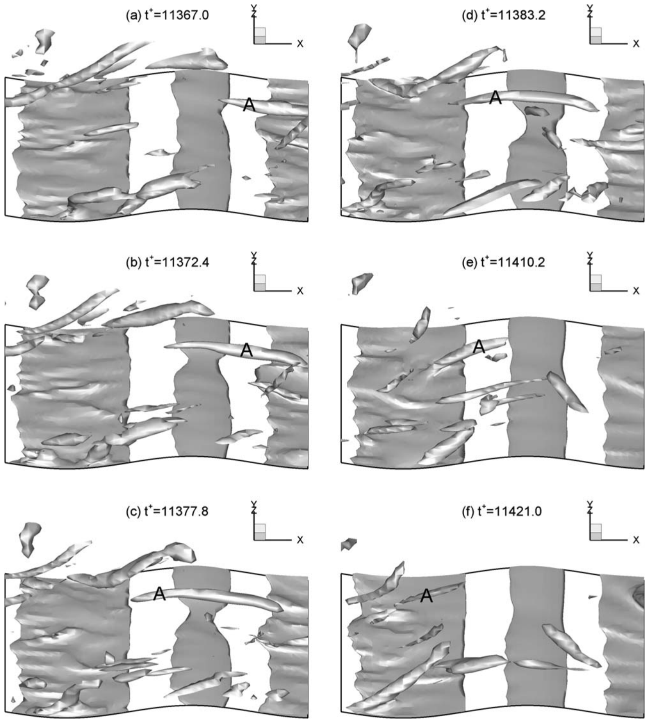

FIG. 24. History of the vortex evolution above the intermediate wave ($c/u_*=14$). The flow field is observed in the wave-following frame, in which the vortical structures travel from right to left. The vortical structures are identified by the isosurface of $\lambda_2=-1$.

D. Evolution of vortical structures over the intermediate wave

In this subsection we discuss the evolution of vortical structures over the intermediate wave. The same as in Sec. III D, we first examine instantaneous vortex fields at successive time frames to illustrate the evolution; we then use the vorticity dynamic equation to show the effects of vortex stretching and turning in the vortex evolution process.

Figure 24 shows the history of the vortex evolution above the intermediate wave ($c/u_*=14$). We re-emphasize that in the wave-following frame, the vortices near the wave surface travel in the $-x$-direction in the cases of intermediate and fast waves [Fig. 4(b)]. Taking the quasistreamwise vortex A as an example, at $t^+=11\,367.0$ [Fig. 24(a)], vortex A is located above the wave trough with its upstream end reaching above the wave crest. Around $t^+=11\,372.4$ [Fig. 24(b)], when vortex A propagates over the leeward face of the wave, it is stretched along the streamwise direction. When vortex A propagates over the wave crest to above the slope upstream of the crest, its upstream end turns downward and is stretched in the vertical direction; meanwhile, its down-

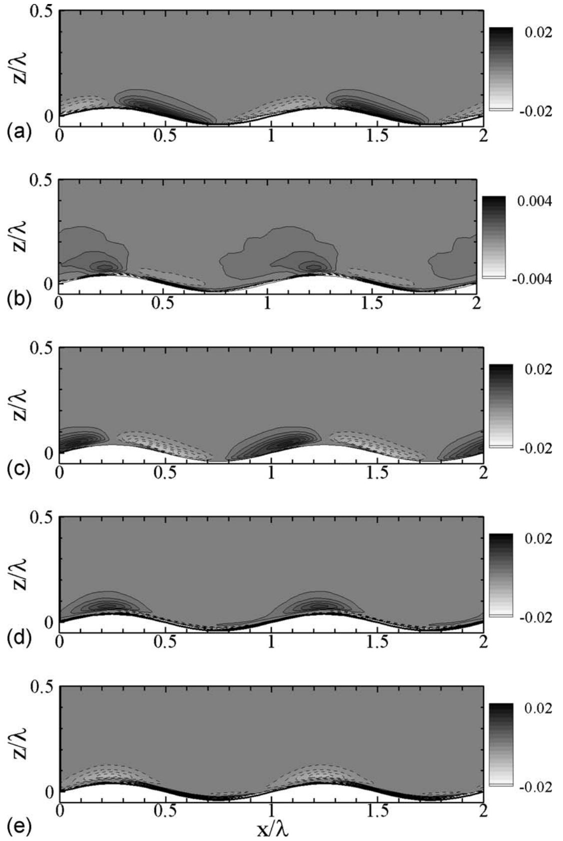

FIG. 25. Contours of vortex stretching and turning terms for the intermediate wave case ($c/u_*=14$) normalized by $(u_*^2/\nu)^2$: (a) vortex stretching of ω_x, $\mathcal{T}_1^1=\langle\omega_x(\partial u/\partial x)\rangle^{1p}$; (b) vortex turning from ω_x to ω_z, $\mathcal{T}_1^3=\langle\omega_x(\partial w/\partial x)\rangle^{3p}$; (c) vortex stretching of ω_z, $\mathcal{T}_3^3=\langle\omega_z(\partial w/\partial z)\rangle^{3p}$; (d) vortex turning from ω_x to ω_z by the strain field S_{31}, $\mathcal{T}_1^3|_{\text{strain}}=\langle\omega_x S_{31}\rangle^{3p}$; and (e) vortex turning from ω_x to ω_z by the rotation field Ω_{31}, $\mathcal{T}_1^3|_{\text{rotation}}=\langle\omega_x\Omega_{31}\rangle^{3p}$. The dashed contour lines represent negative values.

stream end loses intensity over the crest without the support of vortex stretching [Figs. 24(c)–24(e)]. As vortex A continues to propagate to above the next trough [Fig. 24(f)], it loses its intensity and attenuates there.

The above results indicate that the vortex stretching and turning in the (x,z)-plane play an important role in the evolution of the quasistreamwise vortices above the intermediate surface wave. We examine next the vorticity dynamic equations (11) and (12) and plot the terms $\mathcal{T}_1^1$, $\mathcal{T}_3^3$, and $\mathcal{T}_1^3$ in Fig. 25. The further decomposed vortex turning terms $\mathcal{T}_1^3|_{\text{strain}}$ and $\mathcal{T}_1^3|_{\text{rotation}}$ [Eq. (13)] are also plotted for comparison.

Figure 25(a) shows the contours of the vortex stretching term $\mathcal{T}_1^1$. High intensity region of the streamwise stretching is located above the leeward face of the wave. Recall that the vortices propagate in the $-x$-direction in the vicinity of the wave surface [Fig. 4(b)] and the flow velocity is faster above the wave crest. When a streamwise vortex propagates over the leeward face of the wave, its intensity increases due to the vortex stretching along the streamwise direction. Above the wave crest, this stretching ends and the vortex reaches its maximum intensity.

Figure 25(b) shows the vortex turning term $\mathcal{T}_1^3$. The peak of $\mathcal{T}_1^3$ is located slightly upstream above the wave crest. As a streamwise vortex propagates to above the wave crest, its upstream end turns counterclockwise so that the vortex has a vertical component. As the vortex propagates further upstream to above the windward face of the wave, the vertical part of the vortex is enhanced due to the vertical stretching associated with the local gradient $\partial w/\partial z$ [see, e.g., Fig. 21(a)]. This vertical stretching is clearly indicated by the high intensity region of the term $\mathcal{T}_3^3$ of Eq. (12), plotted in Fig. 25(c). Meanwhile, the streamwise part of the vortex attenuates due to vortex compression and viscous dissipation. As a result, the primary direction of the vortex changes from the horizontal direction to the vertical direction. We note that the vertical stretching region in Fig. 25(c) is consistent with the high intensity region of F_z in Fig. 18(a) and the location of the $|\omega_z|$ isosurface in Fig. 20(c).

To further show the vortex turning, we plot in Figs. 25(d) and 25(e) the vortex turning terms associated with the strain field S_{31} and the rotation field Ω_{31}, respectively. Since the magnitude of $\partial w/\partial x$ is much smaller than that of $\partial u/\partial z$, S_{31} and Ω_{31} are close in magnitude but with opposite sign. Therefore, $\mathcal{T}_1^3|_{\text{strain}}$ and $\mathcal{T}_1^3|_{\text{rotation}}$ have similar distributions with opposite sign, and $\mathcal{T}_1^3$ is the summation of the two. We note that although $\mathcal{T}_1^3$ and $\mathcal{T}_1^3|_{\text{strain}}$ have different magnitudes, their similar distributions (high intensity region above the wave crest) indicate consistent descriptions of the vortex turning over the wave crest.

The above results indicate that the evolution of the quasistreamwise vortices above the intermediate wave is consistent with the statistics of the vortex stretching and turning terms in Eqs. (11) and (12). Different from the slow wave case, in which the vortex stretching and turning in the horizontal plane are mainly responsible for the evolution of the vortical structures, the intermediate and fast wave cases are dominated by the vortex stretching and turning processes in the vertical plane. This indicates the significant effect of the wave motion as the wave age increases (i.e., as the wave travels faster).

Finally, we note that Tokuda[30] applied the Görtler instability analysis to gentle winds over water waves, which corresponds to the cases of flows over intermediate and fast waves in our work. His instability analysis predicted the formation of counter-rotating quasistreamwise Görtler vortices above the wave crest. The Görtler instability is a type of centrifugal instability. According to the Rayleigh circulation criterion,[54,55] for the intermediate and fast water wave cases, the flow is unstable and stable above the wave crest and trough, respectively, which coincides with the enhancement and attenuation of the quasistreamwise vortices observed in this study. Other than that work, due to the difficulty of the physical problem associated with the moving wave boundary, there is a lack of study for the vortical structures above the intermediate and fast waves in literature. Our DNS results show that the vortical structures possess unique features such as the downward bending and suggest further study of this problem.

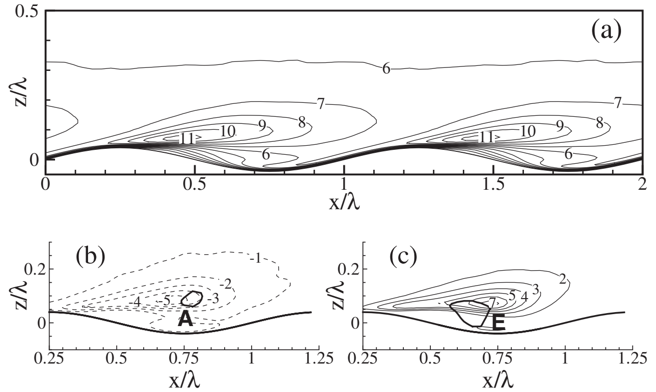

FIG. 26. Turbulent transport of scalar above the slow wave ($c/u_*=2$). In (a), the contours of phase-averaged scalar fluctuation rms values, s'^{rms}, are plotted. In (b) and (c), the contours of scalar fluctuations, s', associated with conditionally averaged vortical structures A and E in Fig. 11 are plotted, respectively. The positions of the vortices are denoted by the thick solid lines. In (b) and (c), the x-z planes are the ones crossing the centerlines of the vortices. All the contour values are normalized by s_*. The dashed contour lines represent negative values. The contour interval is 1.

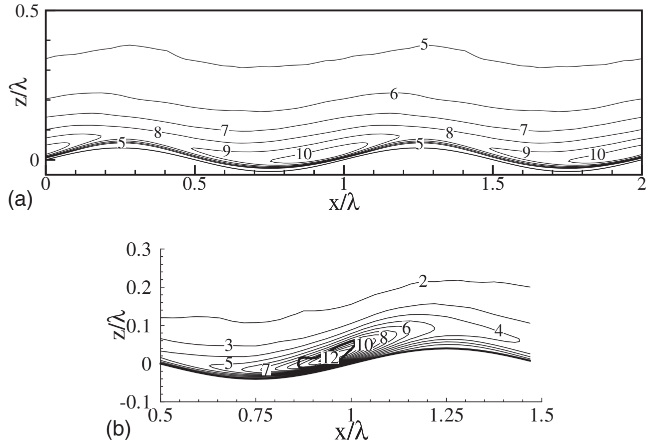

FIG. 27. Turbulent transport of scalar above the intermediate wave ($c/u_*=14$). In (a), the contours of phase-averaged scalar fluctuation rms values, s'^{rms}, are plotted. In (b), the contours of scalar fluctuations, s', associated with conditionally averaged vortical structures in Fig. 20 are plotted. The contour values are normalized by s_*. The contour interval is 1.

V. RELATIONSHIP OF COHERENT VORTICAL STRUCTURES TO TURBULENT TRANSPORT

The coherent vortical structures play an important role in turbulent transport. In previous sections we illustrate their correlation with the Reynolds stress in the turbulent flow over the wave. In this section we discuss transport of a passive scalar in the turbulent flow, and form and friction drag at the wave surface.

A. Scalar transport

To study the effect of coherent vortical structures on scalar transport, we simulate the transport of a passive scalar over the wave as a canonical problem. The concentration of the scalar, s, is governed by the advection-diffusion equation

$$\frac{\partial s}{\partial t}+u_j\frac{\partial s}{\partial x_j}=D_m\frac{\partial^2 s}{\partial x_j\,\partial x_j}. \tag{14}$$

Here, D_m is the molecular diffusivity of the scalar and is related to the kinematic viscosity by $D_m \equiv \nu/\mathrm{Sc}$, with Sc as the Schmidt number. Dirichlet boundary conditions are applied for s at the top and bottom boundaries with $s=1$ at $z=\bar{H}$ and $s=-1$ at $z=z_w$. Using the velocity solved in the DNS, Eq. (14) is simulated using the same numerical method as introduced in Sec. II B. A Schmidt number Sc=2 is used. We use this canonical problem to investigate the fundamentals of scalar transport in the turbulent flow in a way similar to Kim and Moin,[56] Shen *et al.*,[57] Lakehal *et al.*,[58] and Kasagi *et al.*[59]

Figure 26(a) shows the phase-averaged contours of the scalar concentration fluctuation root-mean-square (rms) value, s'^{rms}, for the slow wave case ($c/u_*=2$). The contour value is normalized by a reference friction value s_*, which is defined as $s_*=D_m\partial s/\partial z|_{\mathrm{surface}}/u_*$.[60] The result indicates that the high intensity region of scalar fluctuation starts from the wave crest, extends over the wave trough, and ends above the windward face of the successive downstream wave crest. Figures 26(b) and 26(c) show the contours of the fluctuations of scalar concentration, s', in the conditionally averaged flow field associated with vortical structures A and E in Fig. 11, respectively. The ejection associated with structure A transports low scalar concentration up from the wave surface, resulting in a negative fluctuation of s; on the contrary, the sweep associated with structure E brings high scalar concentration down toward the wave surface, resulting in a positive fluctuation of s. As shown in Figs. 26(b) and 26(c), the scalar fluctuation associated with vortical structures A and E has similar distribution as that in Fig. 26(a), because these vortical structures are responsible for the scalar mixing above the trough of the slow wave.

Similar to what we found in Sec. IV, the fast wave ($c/u_*=25$) case shares considerable similarities with the intermediate wave ($c/u_*=14$) case in terms of scalar transport. Here only the latter are shown due to space limitation. Figure 27(a) shows the phase-averaged contours of s'^{rms} for the intermediate wave case. The high intensity region of scalar fluctuation is located above the wave trough and the windward face of the wave crest. Figure 27(b) shows the contours of s' in the conditionally averaged flow field associated with the vortical structure shown in Fig. 20. The similarity of the scalar fluctuation distributions between Figs. 27(a) and 27(b) indicates that the bent quasistreamwise vortices are responsible for the strong scalar mixing above the windward face of the intermediate wave. As shown earlier in Fig. 20, the vortical structure has a significant vertical component there. Because $\partial s/\partial x<0$ above the windward face, the positive streamwise velocity fluctuation induced by the vertical vorticity results in a positive scalar fluctuation there.

B. Momentum transport at the wave surface

The wind-wave momentum exchange is through the form and friction drag at the wave surface. For slow waves, the form drag is dominant.[19,20] In general, the pressure is

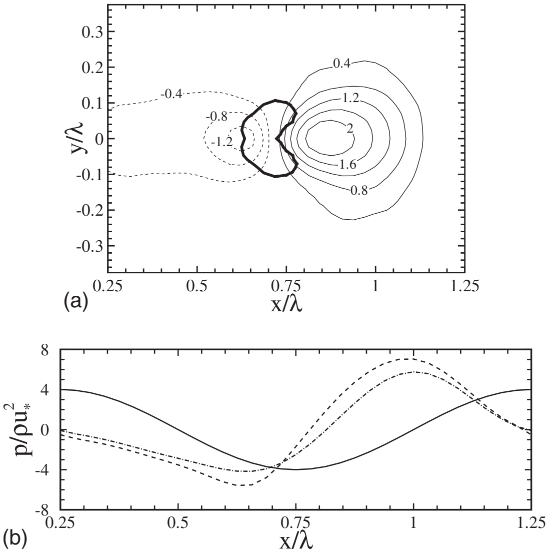

FIG. 28. Distribution of surface pressure associated with the reversed horseshoe vortical structure E in the conditionally averaged flow field of Fig. 10(b). The pressure values are normalized by ρu_*^2. (a) Contours of surface pressure fluctuation p'. (b) Surface pressure profiles at different spanwise locations: – – –, $y/\lambda=0$; –·–, $y/\lambda=0.3$. In (a), the position of the vortical structure E is indicated by the thick solid line; the dashed contour lines represent negative values; the contour interval is 0.4. In (b), the wave surface elevation is indicated by the solid line.

high on the windward face and low on the leeward face, which results in a net momentum transport from wind turbulence to water wave (see, e.g., Ref. 20). We find that this pressure distribution can be largely affected by the vortical structures.

Figure 28 shows the surface pressure distribution in the conditionally averaged flow field associated with the reversed horseshoe vortical structure E shown in Fig. 11 for the slow wave case ($c/u_*=2$). The vertical motions induced by structure E cause negative and positive surface pressure fluctuations upstream and downstream of it, respectively [Fig. 28(a)]. As indicated in Fig. 28(b), the surface pressure fluctuations associated with the vortical structure E enhance the high pressure on the windward face and reduce the low pressure on the leeward face of the water wave, and therefore increase the form drag and the momentum flux from the turbulent flow to the wave.

The dimensionless form drag per unit area is quantified as

$$F_p = \frac{1}{\lambda}\int_0^{\lambda} \frac{p}{\rho u_*^2}\frac{dz_w}{dx}dx.$$

It is found that F_p associated with structure E is 0.59, which is 26% larger than the averaged value 0.47 over the entire wave surface. Occupying 56% of the surface wave profiles, the pressure distribution associated with structure E supports about 70% of the total form drag.

The effect of the quasistreamwise vortices is found mainly on the surface friction drag. Similar to the flat wall boundary layer case,[61] the vertical motions induced by the quasistreamwise vortices greatly enhance the vertical momentum transport[4] and thus the friction drag. For wind over waves, the friction drag becomes important compared to the form drag as the wave age increases (because the pressure distribution becomes more symmetric about the wave crest and thus the form drag reduces significantly).[13–16,19]

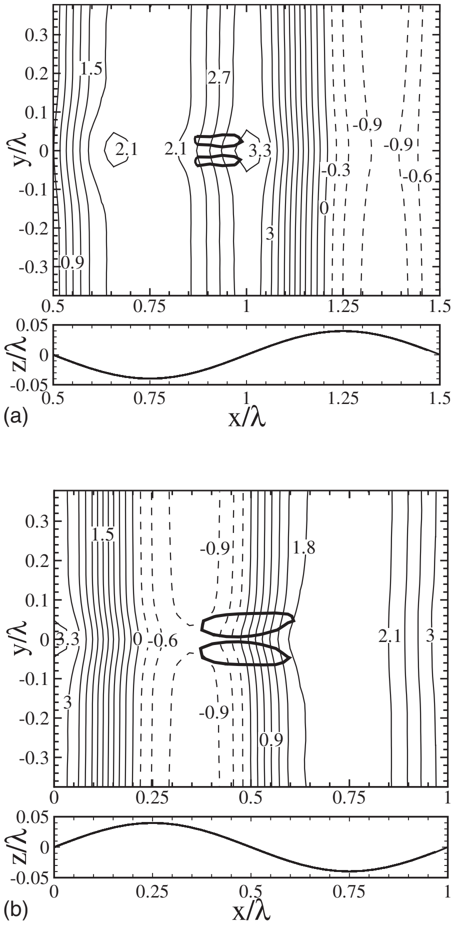

FIG. 29. Conditionally averaged surface shear stress contours associated with the vortical structure in (a) Fig. 20 and (b) Fig. 22(c). The shear stress value is normalized by ρu_*^2. The contour interval is 0.3. The dashed contour lines represent negative values. The position of the vortical structure is indicated by the thick solid line. The bottom profile indicates the elevation of the surface wave.

Here, we show the intermediate wave case ($c/u_*=14$) as an example. Figure 29(a) shows the surface shear stress distribution in the conditionally averaged flow field associated with the bent quasistreamwise vortical structure in Fig. 20 (Q1-related). The positive streamwise velocity fluctuation associated with the vertical component of the vortex pair enhances the streamwise velocity in between and causes 10%–15% increase in the surface shear stress on the windward face between $x/\lambda=0.6$ and 1.1.

Figure 29(b) shows the surface shear stress distribution in the conditionally averaged flow field associated with the quasistreamwise vortical structure in Fig. 22(c) (Q4-related) for the intermediate wave case. The downwelling motion associated with the horizontal vortex pair sweeps the high speed fluid toward the wave surface and causes 10%–20% increase in the shear stress on the leeward face.

VI. CONCLUSIONS

In this study, we perform a DNS based study on the coherent vortices in turbulence over progressive surface waves. To elucidate the characteristics of vortices observed in instantaneous flow field, we first use statistics conditioned on the magnitude of vorticity components to investigate the occurrence of vortical structures with respect to the wave phase and to quantify the primary direction of the vortices. We then use QD-based conditional averaging to study the relationship between vortical structures and turbulent momentum transport above the wave surface. We also use a geometry-based direct sampling method to directly extract characteristic vortices from the turbulence field. With the conditional averaging methods, we are able to obtain useful information on the geometry of the coherent vortical structures, and to illustrate the relationship of vortex features to the waveform and wave motion. Finally, we investigate the evolution of vortices to reveal their generation, transformation, and attenuation processes with respect to the surface wave propagation.

Our study shows that in turbulent flows over progressive waves, there exist unique coherent vortical structures that are highly dependent on the wave motion. In the case of slow surface wave ($c/u_*=2$), it is found that quasistreamwise vortices and reversed horseshoe vortices are the characteristic vortical structures. The quasistreamwise vortices are dominant and have high concentration above the windward face of the wave; they are associated with ejection events. The reversed horseshoe vortices, associated with the sweep events, are concentrated above the wave trough. In the wave-following frame, these vortical structures propagate toward the downstream direction (with respect to the waveform). The results show that over the wave trough, the reversed horseshoe vortices associated with sweeps are transformed into to quasistreamwise vortices; the quasistreamwise vortices then extend and propagate over the wave crest and attenuate before the next trough. Vortex stretching and turning are found to play an essential role in the vortex transformation and evolution process.

Vortical structures over intermediate ($c/u_*=14$) and fast ($c/u_*=25$) waves are substantially different from those in the slow wave case. Because of the relatively large wave phase speed, in the wave-following frame, vortices travel in the upstream direction (with respect to the waveform). Quasistreamwise vortices are found to be the characteristic vortical structure. Over the leeward face of the wave surface, the quasistreamwise vortices extend along the streamwise direction and are associated with the positive Reynolds stress there. Above the wave crest, the vortices are substantially strengthened. As the quasistreamwise vortices propagate over the windward face, their upstream ends have an appreciable downward bending. Due to the vortex bending, the vertical component of vorticity induces streamwise velocity around the vortices, which together with the streamwise gradients of vertical velocity due to the wave motion generate negative Reynolds stress over the windward face of the wave surface. As the wave trough is approached, the bent quasistreamwise vortices interact with the spanwise vortex sheet there and attenuate. The locations for the intensification and attenuation of the quasistreamwise vortices are consistent with the unstable and stable regions of the Görtler instability discussed in literature.

The unique vortical structures over progressive waves reported in this study are found to play an essential role in turbulent transport processes. In this paper, besides the Reynolds stress, we also illustrate the correlation of coherent vortices with scalar mixing and form and friction drag at the wave surface. It is found that the scalar fluctuation magnitude is increased in the regions where the vortices are present. The vertical motion induced by the vortices enhances the transport of the scalar away from and toward the wave surface. For the slow wave case, the reversed horseshoe vortices greatly enhance the pressure on the windward face of the wave, resulting in increased form drag and thus increased momentum input to the wave field. For the intermediate and fast wave cases, the quasistreamwise vortices are found to increase the friction drag.

The results presented in this paper used simulation over a surface with prescribed wave motion. This approach is computationally efficient and has been validated by our additional simulations of dynamically evolving waves using air-water coupled methods. The comparison among different simulation approaches indicates that the essential features of the coherent vortical structures are captured. Nevertheless, it should be pointed out that this study only serves as a first step toward the understanding of vortex dynamics in flows over progressive waves. There are additional factors need to be considered in future study, e.g., the Reynolds number effect, which affects the classification of slow, intermediate, and fast waves.[13,14,21] For this reason, the boundaries and transitions among different wave age cases are not discussed in this paper because the Reynolds number is limited due to the DNS approach used here. To have higher Reynolds numbers, large-eddy simulation will be used. The surface roughness and wave breaking effects should also be considered. Although the surface variation is examined in our LSM simulation, we note that the ripples appearing in spilling breakers may affect the flow structure considerably. To resolve these small-scale structures, more advanced numerical methods using adaptive mesh refinement are required. For plunging breakers and airflow separation, our preliminary results[62] show that spanwise vortical structures appear in the separation zone, which are much more complex than the ones reported in this paper. Further study on these complex cases is needed.

ACKNOWLEDGMENTS

This research was supported by the Office of Naval Research. The Young Investigator award to L.S. is gratefully acknowledged. We would like to thank the referees for their valuable comments that provide us significant help to improve the previous version of this paper.

APPENDIX A: METHODS OF DNS-SNOW COUPLED SIMULATION OF WIND-WAVE INTERACTION

In the DNS-SNOW coupled approach, the motion of the turbulent flow above the surface wave is obtained by the DNS described in Sec. II B. The nonlinear evolution of the wave is captured by the SNOW method[40] based on the HOS method.[41] The HOS directly simulates evolution of the surface elevation z_w and the surface potential Φ^s, which is defined as the surface value of the velocity potential Φ.[63] With a perturbation series of Φ with respect to the wave steepness to the order of M and Taylor series expansions about the mean water level $z=0$,

$$\begin{gathered}\Phi(x,y,z,t) = \sum_{m=1}^{M} \Phi^{(m)}(x,y,z,t), \\ \Phi^s(x,y,t) = \sum_{m=1}^{M} \sum_{\ell=0}^{M-m} \frac{(z_w)^\ell}{\ell!} \left. \frac{\partial^\ell \Phi^{(m)}}{\partial z^\ell} \right|_{z=0},\end{gathered} \tag{A1}$$

and an eigenfunction expansion of each $\Phi^{(m)}$ with N modes,

$$\Phi^{(m)}(x,y,z,t) = \sum_{n=1}^{N} \Phi_n^{(m)}(t) \Psi_n(x,y,z), \quad z \le 0, \tag{A2}$$

the kinematic and dynamic free-surface boundary conditions are written as

$$\begin{aligned}\frac{\partial z_w}{\partial t} = & -\nabla_{\rm h} z_w \cdot \nabla_{\rm h} \Phi^s + (1 + \nabla_{\rm h} z_w \cdot \nabla_{\rm h} z_w) \\ & \times \left[\sum_{m=1}^{M} \sum_{\ell=0}^{M-m} \frac{(z_w)^\ell}{\ell!} \sum_{n=1}^{N} \Phi_n^{(m)}(t) \right. \\ & \left. \times \left| \frac{\partial^{\ell+1}}{\partial z^{\ell+1}} \Psi_n(x,y,z) \right|_{z=0} \right],\end{aligned} \tag{A3}$$

$$\begin{aligned}\frac{\partial \Phi^s}{\partial t} = & -\frac{z_w}{\mathrm{Fr}^2} - \frac{1}{2} \nabla_{\rm h} \Phi^s \cdot \nabla_{\rm h} \Phi^s + D_\Phi - \frac{p_a(x,y)}{\rho_w} \\ & + \frac{1}{2}(1 + \nabla_{\rm h} z_w \cdot \nabla_{\rm h} z_w) \times \left[\sum_{m=1}^{M} \sum_{\ell=0}^{M-m} \frac{(z_w)^\ell}{\ell!} \sum_{n=1}^{N} \Phi_n^{(m)}(t) \right. \\ & \left. \times \left| \frac{\partial^{\ell+1}}{\partial z^{\ell+1}} \Psi_n(x,y,z) \right|_{z=0} \right]^2.\end{aligned} \tag{A4}$$

Here, $\nabla_{\rm h} \equiv \partial/\partial x + \partial/\partial y$, D_Φ is the wave dissipation, p_a is the atmospheric pressure applied at the wave surface representing the wind forcing. Equations (A3) and (A4) are advanced in time with a fourth-order Runge–Kutta scheme. Periodic boundary conditions are applied in the horizontal directions. A Fourier series based pseudospectral method is used for the spatial discretization. The water wave can be either in deep or shallow water condition, which is included in the eigenfunction Ψ_n. Complete review of the scheme, validation, and application of HOS is provided in Refs. 64 and 65.

In DNS-SNOW, the turbulence and wave simulations are dynamically coupled through a fractional step scheme with two-way feedback. At each time step, the HOS simulation provides the surface geometry z_w and velocity $\vec{u}_w$ as a Dirichlet boundary condition for the turbulence field, and the DNS advances in time and obtains pressure distribution p_a on the wave surface; the HOS simulation then uses the surface pressure p_a as the wind forcing in the dynamic free-surface boundary condition (A4) to advance in time. After the above two substeps of alternating advancing, the entire turbulence-and-wave field advances to the next time step. Numerical details and validations of this DNS-SNOW coupled approach can be found in Refs. 42 and 43.

APPENDIX B: LSM FOR AIR–WATER COUPLED MOTION

In the LSM simulation, the air and water together are treated as one fluid system with varying density and viscosity. As described by Sussman *et al.*,[66] the air-water interface is implicitly represented by a level-set function ϕ, which represents the signed distance from the interface. The evolution of ϕ is governed by $\partial\phi/\partial t + \vec{u}\cdot\nabla\phi = 0$. As ϕ evolves in time, the location where $\phi=0$ denotes the interface. For the region where $\phi \neq 0$, a reinitialization procedure of Russo and Smereka[67] is used to preserve the distance property of ϕ.[66]

Following Sussman *et al.*,[66] we write the density and viscosity of the fluid as

$$\begin{gathered}\rho_\varepsilon(\phi) = \rho_a + (\rho_w - \rho_a) H_\varepsilon(\phi) \quad \text{and} \\ \mu_\varepsilon(\phi) = \mu_a + (\mu_w - \mu_a) H_\varepsilon(\phi),\end{gathered} \tag{B1}$$

where $H_\varepsilon(\phi)$ is a smoothed Heaviside function, and the subscripts a and w denote air and water, respectively. The incompressible Navier–Stokes equations for the air-water two-phase flow system can then be written as

$$\begin{aligned}\rho_\varepsilon(\phi)\left(\frac{\partial \vec{u}}{\partial t} + \vec{u}\cdot\nabla\vec{u}\right) = & -\nabla p + \nabla\cdot[2\mu_\varepsilon(\phi) D] \\ & - \sigma\kappa(\phi)\delta_\varepsilon(\phi)\nabla\phi + \rho_\varepsilon(\phi)\vec{g},\end{aligned} \tag{B2}$$

$$\nabla\cdot\vec{u} = 0. \tag{B3}$$

Here, D is the viscous stress tensor, σ is the surface tension, $\kappa(\phi)$ is the curvature of the interface, which satisfies $\kappa(\phi) = \nabla\cdot(\nabla\phi/|\nabla\phi|)$, and $\delta_\varepsilon(\phi)$ is the smoothed delta function, which satisfies $\delta_\varepsilon(\phi) = dH_\varepsilon/d\phi$. In solving Eqs. (B2) and (B3), for spatial discretization, we use a second-order finite-difference scheme on a clustered staggered grid. The time integration is realized through a second-order Runge–Kutta method, with the pressure obtained by a projection method. Numerical details and validations of the current LSM approach can be found in Ref. 44.

APPENDIX C: DIRECT SAMPLING OF VORTICES

To extract vortical structures in the flow field, we use two tag functions $M_s(x,y,z)$ and $M_i(x,y,z)$ to mark the status of data in the sampling procedure. Here, the subscript s stands for "sampling" and i stands for "interior." During the subsequent searching and sampling process, $M_s(x',y',z') = 1$ indicates that the point (x',y',z') has already been identified to be associated with a vortical structure sampled ear-

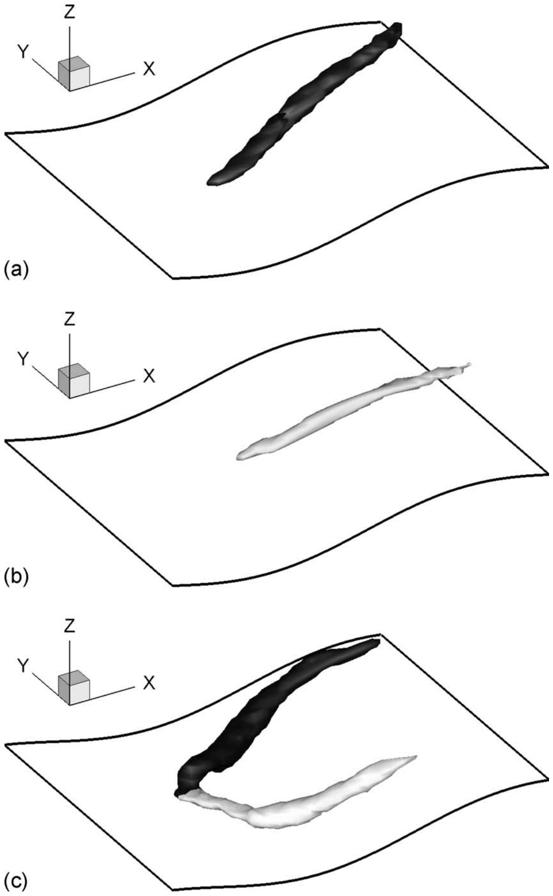

FIG. 30. Samples of the (a) and (b) quasistreamwise, and (c) reversed horseshoe vortices above the slow wave ($c/u_*=2$). The structures with $\omega_x>0$ are marked by the dark color; the structures with $\omega_x<0$ are marked by the light color.

lier; $M_i(x',y',z')=1$ indicates that the point (x',y',z') is inside the vortical structure that is currently under investigation.

We first calculate the λ_2 value in an instantaneous flow field. At the beginning of the search procedure, we initialize the tag functions $M_s(x,y,z)$ and $M_i(x,y,z)$ to be zero everywhere. Then we find the first interior point of the vortical structure by searching for a local maximum of $|\omega_x|$ that also satisfies $\lambda_2<-\varrho$. Here, ϱ is a threshold, which is set to be 1.5 in the present study. The search is performed in the range of $10<((z-z_w)/\lambda)^+<40$, where quasistreamwise vortices occur as shown in Fig. 8. Once such an interior point (referred to as point O) is found, set $M_i(x_O,y_O,z_O)=1$ at this point, and then check all the neighboring grid points of point O. If a neighboring point P satisfies $M_s(x_P,y_P,z_P)=0$ and $\lambda_2(x_P,y_P,z_P)<-\varrho$, it is considered to be an interior point of the current vortical structure. We set $M_i(x_P,y_P,z_P)=1$ and move on to check the neighboring points of point P. This search is repeated until no new interior point can be found. After the above search, all the grid points belonging to the vortical structure that contains the original point O have been marked by $M_i=1$. The geometry of the current vortical structure is checked based on the spatial distribution of the points belonging to it. If the vortical structure is mainly in the streamwise direction, we take it as a sample of quasistreamwise vortex. We then set $M_s=1$ for all the interior points of the current sample, reinitialize M_i to be zero everywhere, and repeat the above search procedure for the next sample until no new sample can be found in the current instantaneous flow field.

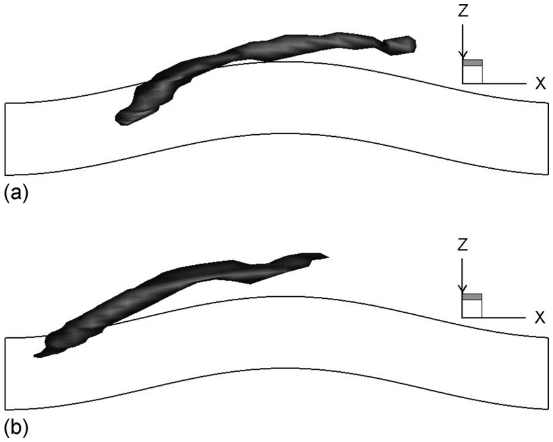

FIG. 31. Samples of the quasistreamwise vortices above the intermediate wave ($c/u_*=14$).

By following the above procedure, we obtain samples of quasistreamwise vortices in an instantaneous flow field. Figures 30(a) and 30(b) show two typical quasistreamwise vortices above the slow wave ($c/u_*=2$). The result indicates that this method is able to extract the target vortical structures from the complex background flow field (Fig. 5). It is also found that different instantaneous vortices usually have different inclination angles, and their downstream ends may point to different directions. Figure 31 shows two typical samples of the quasistreamwise vortices above the intermediate wave ($c/u_*=14$).

For the reversed horseshoe vortices, the direct sampling method can also be used to obtain samples for conditional averaging. Compared to the quasistreamwise case, two modifications are needed in the procedure: (i) search the local maximum of $|\omega_y'|$ instead of $|\omega_x|$ to find the first interior point of the vortical structure; and (ii) check if the geometry is of reversed horseshoe shape. Figure 30(c) shows a typical example of the reversed horseshoe vortex over the slow wave.

[1] J. C. R. Hunt, S. Leibovich, and K. J. Richards, "Turbulent shear flows over low hills," Q. J. R. Meteorol. Soc. **114**, 1435 (1988).

[2] K. Krettenauer and U. Schumann, "Numerical simulation of turbulent convection over wavy terrain," J. Fluid Mech. **237**, 261 (1992).

[3] W. Gong, P. A. Taylor, and A. Dörnbrack, "Turbulent boundary-layer flow over fixed aerodynamically rough two-dimensional sinusoidal waves," J. Fluid Mech. **312**, 1 (1996).

[4] V. De Angelis, P. Lombardi, and S. Banerjee, "Direct numerical simulation of turbulent flow over a wavy wall," Phys. Fluids **9**, 2429 (1997).

[5] D. S. Henn and R. I. Sykes, "Large-eddy simulation of flow over wavy surfaces," J. Fluid Mech. **383**, 75 (1999).

[6] R. J. Calhoun and R. L. Street, "Turbulent flow over a wavy surface: Neutral case," J. Geophys. Res. **106**, 9277, doi:10.1029/2000JC900133 (2001).

[7] Y.-H. Tseng and J. H. Ferziger, "Large-eddy simulation of turbulent wavy boundary flow—Illustration of vortex dynamics," J. Turbul. **5**, N34 (2004).

[8] S. Nakagawa and T. J. Hanratty, "Particle image velocimetry measurements of flow over a wavy wall," Phys. Fluids **13**, 3504 (2001).

[9] A. Günther and P. R. von Rohr, "Large-scale structures in a developed flow over a wavy wall," J. Fluid Mech. **478**, 257 (2003).

[10] S. E. Belcher and J. C. R. Hunt, "Turbulent shear flow over slowly moving waves," J. Fluid Mech. **251**, 109 (1993).

[11] J. E. Cohen and S. E. Belcher, "Turbulent shear flow over fast-moving waves," J. Fluid Mech. **386**, 345 (1999).

[12] M. J. Lighthill, "Physical interpretation of the mathematical theory of wave generation by wind," J. Fluid Mech. **14**, 385 (1962).

[13] P. P. Sullivan, J. C. McWilliams, and C.-H. Moeng, "Simulation of turbulent flow over idealized water waves," J. Fluid Mech. **404**, 47 (2000).

[14] J. F. Meirink and V. K. Makin, "Modeling low-Reynolds-number effects in the turbulent air flow over water waves," J. Fluid Mech. **415**, 155 (2000).

[15] P. Y. Li, D. Xu, and P. A. Taylor, "Numerical modeling of turbulent airflow over water waves," Boundary-Layer Meteorol. **95**, 397 (2000).

[16] N. Kihara, H. Hanazaki, T. Mizuya, and H. Ueda, "Relationship between airflow at the critical height and momentum transfer to the traveling waves," Phys. Fluids **19**, 015102 (2007).

[17] C.-T. Hsu, E. Y. Hsu, and R. L. Street, "On the structure of turbulent flow over a progressive water wave: Theory and experiment in a transformed, wave-following co-ordinate system," J. Fluid Mech. **105**, 87 (1981).

[18] W. J. Plant, "A relationship between wind stress and wave slope," J. Geophys. Res. **87**, 1961, doi:10.1029/JC087iC03p01961 (1982).

[19] C. Mastenbroek, V. K. Makin, M. H. Garat, and J. P. Giovanangeli, "Experimental evidence of the rapid distortion of turbulence in the air flow over water waves," J. Fluid Mech. **318**, 273 (1996).

[20] M. A. Donelan, A. V. Babanin, I. R. Young, and M. L. Banner, "Wave-follower field measurements of the wind-input spectral function. Part 2: Parameterization of the wind input," J. Phys. Oceanogr. **36**, 1672 (2006).

[21] D. Yang and L. Shen, "Direct-simulation-based study of turbulent flow over various waving boundaries," J. Fluid Mech. (to be published).

[22] J. Kim, "On the structure of wall-bounded turbulent flows," Phys. Fluids **26**, 2088 (1983).

[23] P. Moin and J. Kim, "The structure of the vorticity field in turbulent channel flow. Part 1. Analysis of instantaneous fields and statistical correlations," J. Fluid Mech. **155**, 441 (1985).

[24] S. K. Robinson, "Coherent motions in the turbulent boundary layer," Annu. Rev. Fluid Mech. **23**, 601 (1991).

[25] R. J. Adrian, "Hairpin vortex organization in wall turbulence," Phys. Fluids **19**, 041301 (2007).

[26] P. Hall and N. J. Horseman, "The linear inviscid secondary instability of longitudinal vortex structures in boundary layers," J. Fluid Mech. **232**, 357 (1991).

[27] J. D. Swearingen and R. F. Blackwelder, "The growth and breakdown of streamwise vortices in the presence of a wall," J. Fluid Mech. **182**, 255 (1987).

[28] R. D. Moser and P. Moin, "The effects of curvature in wall-bounded turbulent flows," J. Fluid Mech. **175**, 479 (1987).

[29] H. Görtler, "Über eine drei dimensional instabilität Laminarer grenzschichten an knokaven wänden," Nachr. Ges. Wiss Gättingen **2**, 1 (1945).

[30] M. Tokuda, "Taylor–Görtler vortices expected in the air flow on sea surface waves—I," J. Oceanogr. Soc. Jpn **28**, 242 (1972).

[31] S. E. Belcher and J. C. R. Hunt, "Turbulent flow over hills and waves," Annu. Rev. Fluid Mech. **30**, 507 (1998).

[32] L. Shen, X. Zhang, D. K. P. Yue, and M. S. Triantafyllou, "Turbulent flow over a flexible wall undergoing a streamwise traveling wave motion," J. Fluid Mech. **484**, 197 (2003).

[33] J. Kim and P. Moin, "Application of a fractional-step method to incompressible Navier–Stokes equations," J. Comput. Phys. **59**, 308 (1985).

[34] J. Kim, P. Moin, and R. D. Moser, "Turbulence statistics in fully developed channel flow at low Reynolds number," J. Fluid Mech. **177**, 133 (1987).

[35] A. K. M. F. Hussain and W. C. Reynolds, "The mechanics of an organized wave in turbulent shear flow," J. Fluid Mech. **41**, 241 (1970).

[36] H. Tennekes and J. L. Lumley, *A First Course in Turbulence* (MIT Press, Cambridge, 1972).

[37] J. Jeong and F. Hussain, "On the identification of a vortex," J. Fluid Mech. **285**, 69 (1995).

[38] J. Zhou, R. J. Adrian, S. Balachandar, and T. M. Kendall, "Mechanisms for generating coherent packets of hairpin vortices in channel flow," J. Fluid Mech. **387**, 353 (1999).

[39] P. Chakraborty, S. Balachandar, and R. J. Adrian, "On the relationships between local vortex identification schemes," J. Fluid Mech. **535**, 189 (2005).

[40] D. K. P. Yue, "Nonlinear wave environments for ship analysis," Proceedings of the 27th Symposium on Naval Hydrodynamics, Seoul, Korea, 5–10 October 2008, p. 297.

[41] D. G. Dommermuth and D. K. P. Yue, "A high-order spectral method for the study of nonlinear gravity waves," J. Fluid Mech. **184**, 267 (1987).

[42] L. Shen, D. Yang, and D. K. P. Yue, "Coupled wind-wave prediction for ship motion," Proceedings of the 27th Symposium on Naval Hydrodynamics, Seoul, Korea, 5–10 October 2008, p. 48.

[43] L. Shen, *Notes on Numerical Fluid Mechanics and Multidisciplinary Design* (Springer, Berlin, in press).

[44] K. L. Hendrickson, "Navier-Stokes simulation of steep breaking water waves with a coupled air-water interface," Ph.D. thesis, Massachusetts Institute of Technology, 2004.

[45] P. C. Chang, E. J. Plate, and G. M. Hidy, "Turbulent air flow over the dominant component of wind-generated water waves," J. Fluid Mech. **47**, 183 (1971).

[46] R. F. Blackwelder and R. E. Kaplan, "On the wall structure of the turbulent boundary layer," J. Fluid Mech. **76**, 89 (1976).

[47] J. Kim and P. Moin, "The structure of the vorticity field in turbulent channel flow. Part 2. Study of ensemble-averaged fields," J. Fluid Mech. **162**, 339 (1986).

[48] R. J. Adrian and P. Moin, "Stochastic estimation of organized turbulent structure: Homogeneous shear flow," J. Fluid Mech. **190**, 531 (1988).

[49] P. Moin and R. Moser, "Characteristic-eddy decomposition of turbulence in a channel," J. Fluid Mech. **200**, 471 (1989).

[50] J. W. Brooke and T. J. Hanratty, "Origin of turbulence-producing eddies in a channel flow," Phys. Fluids A **5**, 1011 (1993).

[51] W. R. C. Phillips, Z. Wu, and J. L. Lumley, "On the formation of longitudinal vortices in a turbulent boundary layer over wavy terrain," J. Fluid Mech. **326**, 321 (1996).

[52] A. D. D. Craik, "The generation of Langmuir circulations by an instability mechanism," J. Fluid Mech. **81**, 209 (1977).

[53] S. Leibovich, "Convective instability of stably stratified water in the ocean," J. Fluid Mech. **82**, 561 (1977).

[54] Lord Rayleigh, *Scientific Paper 6* (Cambridge University Press, Cambridge, 1916), p. 447.

[55] W. S. Saric, "Görtler vortices," Annu. Rev. Fluid Mech. **26**, 379 (1994).

[56] J. Kim and P. Moin, "Transport of passive scalars in a turbulent channel flow," Proceedings of the Sixth Symposium on Turbulent Shear Flows, Toulouse, France, 7–9 September 1987.

[57] L. Shen, G. S. Triantafyllou, and D. K. P. Yue, "Mixing of a passive scalar near a free surface," Phys. Fluids **13**, 913 (2001).

[58] D. Lakehal, M. Fulgosi, G. Yadigaroglu, and S. Banerjee, "Direct numerical simulation of turbulent heat transfer across a mobile, sheared gas-liquid interface," ASME J. Heat Transfer **125**, 1129 (2003).

[59] N. Kasagi, Y. Tomita, and A. Kuroda, "Direct numerical simulation of passive scalar field in a turbulent channel flow," ASME J. Heat Transfer **114**, 598 (1992).

[60] J. Magnaudet and I. Calmet, "Turbulent mass transfer through a flat shear-free surface," J. Fluid Mech. **553**, 155 (2006).

[61] H. Choi, P. Moin, and J. Kim, "Active turbulence control for drag reduction in wall-bounded flows," J. Fluid Mech. **262**, 75 (1994).

[62] L. Shen, "Phase-resolved simulation of turbulence–wave interaction for deterministic prediction of wavefield evolution," Proceedings of Workshop on Deterministic Measurement and Simulation of Ocean waves, Delft, The Netherlands, May 2009.

[63] V. E. Zakharov, "Stability of periodic wave of finite amplitude on the surface of a deep fluid," J. Appl. Mech. Tech. Phys. **2**, 190 (1968).

[64] C. C. Mei, M. Stiassnie, and D. K. P. Yue, *Theory and Applications of Ocean Surface Waves. Part 2. Nonlinear Aspects* (World Scientific, Hackensack, New Jersey, 2005).

[65] W.-T. Tsai and D. K. P. Yue, "Computation of nonlinear free-surface flows," Annu. Rev. Fluid Mech. **28**, 249 (1996).

[66] M. Sussman, E. Fatemi, P. Smereka, and S. Osher, "An improved level set method for incompressible two-phase flows," Comput. Fluids **27**, 663 (1998).

[67] G. Russo and P. Smereka, "A remark on computing distance functions," J. Comput. Phys. **163**, 51 (2000).